Effective Computational Route to Vibrational Optical Activity Spectra of Chiral Molecules in Aqueous Solution

Tommaso Giovannini, Gianluca Del Frate, Piero Lafiosca, and Chiara Cappelli*

Scuola Normale Superiore, Piazza dei Cavalieri 7, 56126 Pisa, Italy.

E-mail: chiara.cappelli@sns.it

Abstract

We present a computational methodology, based on a polarizable Quantum Mechanical (QM)/Molecular Mechanics (MM) approach to accurately compute Vibrational Optical Activity (VOA) spectra of chiral systems. The approach is applied to the calculation of Infrared (IR), Vibrational Circular Dichroism (VCD), Raman and Raman Optical Activity (ROA) spectra of aqueous solutions of (L)-Methyl Lactate and (S)-Glycidol. Remarkable agreement between calculations and experiments is reported, showing the reliability and accuracy of the methodology, especially with respect to standard continuum solvation approaches.

1 Introduction

Chiroptical spectroscopic methods are nowadays the most useful tools to study chiral systems and assign their molecular absolute configuration. Chiroptical spectral signals arise from the differential response of the chiral system to polarized light, either in absorption/emission or scattering of the right and left components of the circularly polarized light. Basically, two different families of chiroptical molecular responses have been developed, focusing on the electronic or vibrational molecular degrees of freedom. The former, such as the Optical Rotation Dispersion (ORD) and the Electronic Circular Dichroism (ECD), provide relatively little molecular information in comparison with vibrational chiroptical spectroscopies, i.e. Vibrational Circular Dichroism (VCD) and Raman Optical Activity (ROA), because there are many more bands sensitive to the details of the molecular structure in the vibrational domain than for the different electronic states accessible to experimental investigations.[1–3] VCD and ROA, which are collectively named as Vibrational Optical Activity (VOA), have demonstrated high reliability and a wide range of applicability, as it has been amply documented by recent papers.[2,4–13]

VOA has been so far mostly employed to study biomolecules or natural biopolymers in solution,[1–3,14] however their horizons are broadening, as they have also applied to the study of structural patterns in synthetic chiral polymers,[15] fibrillar patterns,[16] ionic liquids[17] and the transfer of chirality from a chiral analyte to an achiral molecule in the vicinity of a plasmon resonance of an achiral metallic nanostructure.[18] The wide applicability of VOA is due to its sensitivity to the local environment experienced by the chiral system. However, if such a feature is beneficial for the experimental investigation, it is a severe issue to deal with in the development of reliable modeling strategies. In fact, the unambiguous assignment of VOA spectra to enantiomers and structural patterns is only possible by a subtle interplay of experiment and theory, which requires the availability of reliable and algorithms for predicting the spectroscopic signals in a computationally viable manner.[19,20] Such algorithms, cannot neglect the presence of the environment, because that can cause a totally wrong reproduc-

tion of the molecular chiroptical signal, up to impede a correct assignment of the absolute configuration.[21,22] For this reason, in the last years significant advances have been made in the coupling of reliable approaches to treat environmental effects and *ab initio* Quantum Mechanical (QM) methods to predict these signals.[1–3,11,19,21,23–41]

The most successful approaches in this field belong to the family of the so-called focused models, where the system is divided in two portions: a target molecule (e.g. the solute in case of solvated systems), which is responsible for the spectral signal and is treated accurately with *ab initio* QM methods, and the environment (e.g. the solvent), which is treated at a lower level, usually by resorting to classical physics. By resorting to such approaches, the molecule/environment interactions and their effects on the molecular structure and properties are accurately captured.[21,22] The most renowned focused models belong to the family of QM/Classical approaches, in which the classical portion can keep an atomistic description (giving rise to QM/Molecular Mechanics(MM) models)[42–46] or even be blurred to a continuum.[47–50]

Continuum solvation approaches, and the Polarizable Continuum Model (PCM) in particular, have been extended to VOA several years ago.[33,51] Nowadays, they represent the most used strategy to include the effects of the environment on calculated VOA spectra, due to their low computational cost. However, whenever the target system and the environment strongly interact, the mean-field continuum approach may fail and the use of discrete approaches, able to account for specific and directional interactions, is compulsory. This is for instance the case of a solute-solvent couple interacting thorugh hydrogen bonding.[52,53]

In such cases, the limitations of continuum strategies can be effectively overcome by using explicit QM/MM approaches,[31,43] and in particular those accounting for the mutual polarization between the QM and MM moieties of the system, i.e. the so-called polarizable QM/MM methods.[22,53–61]

Although several papers have addressed the prediction of electronic response properties in the polarizable QM/MM approach,[53,59,62,63] much less work has been done to extend such

approaches to vibrational spectroscopies (IR, Raman) and especially VOA. To the best of our knowledge, the only polarizable QM/MM currently able to calculate such spectra is the QM/Flucuating Charges (FQ) model, based on the Polarizable Fluctuating Charges (FQ) Force Field,[64–66] which has recently been extended to several molecular properties and spectroscopies by some of the present authors.[20,22,52,67–72]

To illustrate our approach, and report simultaneously for the first time on the IR, Raman, VCD and ROA spectra calculated with our method, two chiral systems are here considered, i.e. aqueous solutions of (L)-Methyl Lactate (ML) and (S)-Glycidol (GL) (Figure 1). For both systems, experimental IR, Raman, VCR and ROA spectra have been reported in the literature, as they have been employed as test systems to get a deep understanding of their intermolecular interaction with water.[4,7,73–75] In fact, their vibrational spectra have been reported to be strongly modified by the presence of the surrounding aqueous solution, giving rise to several specific features due to hydrogen bonding interactions between the chiral systems and the nearby water molecules.[4–7,74,75]

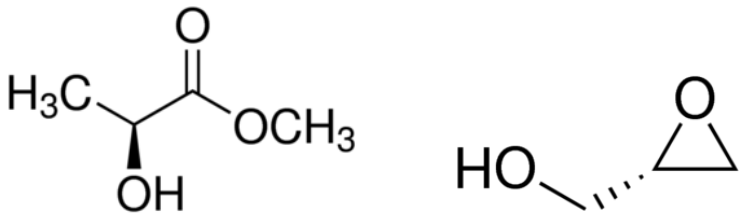

Figure 1: (L)-Methyl Lactate and (S)-Glycidol molecular structures

The paper is organized in the following way. In the next section the computational protocol for the calculation of vibrational spectra with the fully polarizable QM/FQ approach is recalled. Then, its application to IR, Raman, VCD and ROA spectra of (L)-Methyl Lactate and (S)-Glycidol is reported, with particular emphasis on the comparison between calculations and experiments. A section focusing on the conclusions of this work and its future perspectives end the manuscript.

2 Methodology

The aim of this section is to introduce the reader with the computational protocol for the evaluation of vibrational (IR, VCD, Raman and ROA) spectra within the fully polarizable QM/FQ approach. The theoretical fundamentals of the method are briefly recalled in the next section, as well as the definition of the computational protocol allowing the calculation of the spectra for a given chemical system.

2.1 QM/FQ Approach to Vibrational Spectra

The QM/FQ model is a multiscale approach defined in the framework of focused models. When it is applied to molecular systems in solution, this means treating the solute at QM level of theory, whereas the solvent is described by means of the polarizable Fluctuating Charge force field. In Figure 2, a schematic picture of the partitioning is shown.

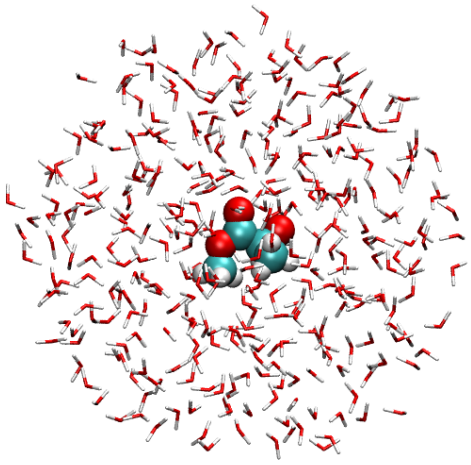

Figure 2: Schematic picture of the partition in the QM/FQ model. The van der Waals spheres represent the QM portion, whereas the water molecules the FQ one.

The FQ force field[22,76] represents each atom of the MM portion with a set of fluctuating charges. The polarization arises from the difference of electronegativities between each atom in the electronegativity equalization principle (EEP)[77,78] framework. The EEP states that, at equilibrium, the instantaneous electronegativity χ of each atom have the same value,[77,79]

which give a minimization principle in a variational meaning of the term.

The FQs (q) can be defined as those minimizing the following functional[76]

$$\begin{aligned} F(\mathbf{q},\lambda) =& \sum_{\alpha,i} q_{\alpha i}\chi_{\alpha i} + \frac{1}{2}\sum_{\alpha,i}\sum_{\beta,j} q_{\alpha i}J_{\alpha i,\beta j}q_{\beta j} + \sum_{\alpha}\lambda_{\alpha}(\sum_{i} q_{\alpha i} - Q_{\alpha}) \\ =& \mathbf{q}^{\dagger}\boldsymbol{\chi} + \frac{1}{2}\mathbf{q}^{\dagger}\mathbf{J}\mathbf{q} + \boldsymbol{\lambda}^{\dagger}\mathbf{q} \end{aligned} \tag{1}$$

where the Greek indices α run over molecules and the Latin ones i over the atoms of each molecule. $\boldsymbol{\lambda}$ is a set of Lagrangian multipliers used to impose charge conservation constraints. $\mathbf{J}$ is the charge interaction kernel: there are several ways to treat this term[78,80–82] and in our implementation the Ohno kernel[83] is exploited.

By following the general philosophy of the so-called "focused" models, in the QM/FQ model, a classical electrostatic interaction between the FQs and the QM density is considered:[67]

$$E_{\mathrm{QM/FQ}} = \sum_{i=1}^{N_q} V_{\mathrm{QM}}[\rho](\mathbf{r}_i)q_i \tag{2}$$

where $V_{\mathrm{QM}}[\rho](\mathbf{r}_i)$ is the electrostatic potential due to the QM density of charge at the i-th FQ q_i placed at $\mathbf{r}_i$. Notice that some of the authors recently extended the present model to the inclusion of non-electrostatic interactions, although they are not considered in the present work.[84] If a Self Consistent Field (SCF) description of the QM portion is adopted, the global QM/MM energy functional reads:[67,68,85]

$$\mathcal{E}[\mathbf{P},\mathbf{q},\boldsymbol{\lambda}] = \mathrm{tr}\mathbf{h}\mathbf{P} + \frac{1}{2}\mathrm{tr}\mathbf{P}\mathbf{G}(\mathbf{P}) + \mathbf{q}^{\dagger}\boldsymbol{\chi} + \frac{1}{2}\mathbf{q}^{\dagger}\mathbf{J}\mathbf{q} + \boldsymbol{\lambda}^{\dagger}\mathbf{q} + \mathbf{q}^{\dagger}\mathbf{V}(\mathbf{P}) \tag{3}$$

where $\mathbf{h}$ and $\mathbf{G}$ are the one and two electron contributions to the energy and Fock operator, and $\mathbf{P}$ is the density matrix. The FQs consistent with the QM density are obtained by solving the following equation

$$\mathbf{D}\mathbf{q}_{\boldsymbol{\lambda}} = -\mathbf{C}_Q - \mathbf{V}(\mathbf{P}) \tag{4}$$

which includes the coupling term $\mathbf{V}(\mathbf{P})$ between the QM and MM moieties.

Once the basic QM/FQ approach is set up, the extension to spectroscopic and transition properties is obtained through the definition of analytical energy derivatives and response equations to electric and magnetic perturbations.[85] We refer the reader to refs.[22,67–69] for major details on the implementation and to ref.[72] for major details on VCD spectra. Extension of the QM/FQ model to the analytical evaluation of Raman and Raman Optical Activity has recently been presented by some of the present authors.[20]

The resorting to the physical framework of the so-called "focused models" implies that external perturbations (i.e., electric/magnetic fields and/or a nuclear displacement) only act on the QM portion of the system, whereas the environment is only indirectly affected through the perturbation on the QM density. In vibrational spectroscopy, the focusing on the QM portion of the system means that the geometric displacements of the MM molecules are not taken into account; this framework is well-defined within the Partial Hessian Vibrational Approach (PHVA).[86–88] The calculation of vibrational frequencies in the harmonic regime requires the evaluation of energy second derivatives. They can be obtained by differentiating twice Equation 1 with respect to x, y perturbations:[68]

$$\begin{aligned}\mathcal{E}^{xy} &= \sum_{\mu\nu}\left[h^{xy}_{\mu\nu}+\frac{1}{2}G^{(xy)}_{\mu\nu}(\mathbf{P})+\mathbf{q}^{\dagger}\mathbf{V}^{xy}_{\mu\nu}\right]P_{\mu\nu}-\text{tr }\mathbf{W}\mathbf{S}^{xy}-\text{tr }\mathbf{W}^{y}\mathbf{S}^{x}\\ &+ \sum_{\mu\nu}\left[h^{x}_{\mu\nu}+G^{(x)}_{\mu\nu}(\mathbf{P})+\mathbf{q}^{\dagger}\mathbf{V}^{x}_{\mu\nu}\right]P^{y}_{\mu\nu}+\sum_{\mu\nu}\mathbf{q}^{y\dagger}\mathbf{V}^{x}_{\mu\nu}P_{\mu\nu}\end{aligned}$$

where μ, ν are atomic basis functions, $\mathbf{W}$ is the energy-weighted density matrix, and $\mathbf{S}$ is the overlap matrix. Notice that Equation 5 requires the computation of the perturbed density matrix, which is accessible through a Coupled Perturbed Hartree-Fock or Kohn-Sham (CPHF/KS) procedure by solving a modified set of equations including FQ terms.[67,68]

In the construction of the CPHF equations the Fock matrix derivative is used:

$$\begin{aligned}\tilde{\mathbf{F}}^x &= \mathbf{h}^x + \mathbf{G}^{(x)}(\mathbf{P}) + \mathbf{q}^\dagger \mathbf{V}^x + \mathbf{G}(\mathbf{P}^x) + \mathbf{V}^\dagger \mathbf{q}^x \\ &= \mathbf{F}^{(x)} + \mathbf{q}^\dagger \mathbf{V}^x + \mathbf{G}(\mathbf{P}^x) + \mathbf{V}^\dagger \mathbf{q}^x \end{aligned} \tag{5}$$

which is included in the $\tilde{\mathbf{Q}}_X$ and $\tilde{\mathbf{Q}}_Y$ terms of the Casida Equation:

$$\begin{pmatrix} \tilde{\mathbf{A}} & \tilde{\mathbf{B}} \\ \tilde{\mathbf{B}}^* & \tilde{\mathbf{A}}^* \end{pmatrix} \begin{pmatrix} \mathbf{X} \\ \mathbf{Y} \end{pmatrix} = \begin{pmatrix} \tilde{\mathbf{Q}}_X \\ \tilde{\mathbf{Q}}_Y \end{pmatrix} \tag{6}$$

The solution of this set of equations yields the density matrix derivatives, $P^x_{jb} = X_{jb}$ and $P^x_{bj} = Y_{jb}$. Eq.5 also allows the calculation of IR intensities, if x, y are specified as nuclear coordinate and electric field component. In case of magnetic perturbations, other terms need to be considered to assure gauge invariance in the computed results. We refer the interested reader to ref.[69] for further details. VCD intensities are proportional to Rotational Strengths (RS), i.e. the imaginary part of the product between the electric and the magnetic dipole moments. RS can be expressed in terms of two tensors, namely the Atomic Polar Tensor (APT) and the Atomic Axial Tensor (AAT), which are defined as:[3,26–29]

$$\begin{aligned}(\mathrm{APT})^\lambda_{\alpha\beta} &= E^\lambda_{\alpha\beta} + N^\lambda_{\alpha\beta} = \\ &= 2\left\langle \left(\frac{\partial \Psi_G}{\partial X_{\lambda\alpha}}\right)_{R_0} \middle| (\mu^e_{el})_\beta \middle| \Psi^0_G \right\rangle + Z_\lambda e \delta_{\alpha\beta} \end{aligned} \tag{7}$$

$$\begin{aligned}(\mathrm{AAT})^\lambda_{\alpha\beta} &= I^\lambda_{\alpha\beta} + J^\lambda_{\alpha\beta} = \\ &= \left\langle \left(\frac{\partial \Psi_G}{\partial X_{\lambda\alpha}}\right)_{R^0} \middle| \left(\frac{\partial \Psi_G}{\partial B_\beta}\right)_{B_\beta = 0} \right\rangle + \frac{i}{4hc} \sum \varepsilon_{\alpha\beta\gamma} R^0_{\lambda\gamma} (Z_\lambda e) \end{aligned} \tag{8}$$

where μ^e_{el} is the electronic part of μ_{el} while $Z_\lambda e$ and R^0_λ are the charge and position of nucleus λ at the equilibrium geometry R^0. Ψ_G is the wave function of the ground electronic

state while $(\partial\Psi_G/\partial X_{\lambda\alpha})$ and $(\partial\Psi_G/\partial B_\beta)$ are the derivatives of the wave function with respect to nuclear displacement and magnetic field, respectively. The former enters into a vibrational transition moment; the latter is appropriate to a magnetic dipole transition moment. FQ contributions affect the wavefunction and its derivatives. In particular, by solving the CPHF/CPKS equations (modified according to the Gauge Including Atomic Orbital–GIAO approach) taking into account FQ contributions, the APT and AAT in the QM/FQ framework are obtained.

By exploiting the Placzek approach within the double harmonic approximation, Raman and ROA intensities are obtained in terms of the geometric derivatives of the electric dipole-electric dipole polarizability α^x, electric dipole-electric quadrupole polarizability A^x and electric dipole-magnetic dipole polarizability G'^x. In particular, Raman intensities depend only on α^x, whereas ROA intensities depend on α^x, A^x and G'^x. In the following equations the QM/FQ contributions to these quantities are reported. We refer the interested reader to Ref.[20] for further details.

$$\alpha^x_{QM/FQ} = \sum_{\mu\nu}\left[\mathbf{q}^\dagger(\mathbf{P}^{e'}(\omega'))\mathbf{V}^x_{\mu\nu}P^e_{\mu\nu}(\omega)\right] + \sum_{\mu\nu}\left[\mathbf{q}^\dagger(\mathbf{P}^{e}(\omega))\mathbf{V}^x_{\mu\nu}P^{e'}_{\mu\nu}(\omega')\right] \tag{9}$$

$$A^x(\omega)_{QM/FQ} = \sum_{\mu\nu}\left[\mathbf{q}^\dagger(\mathbf{P}^{e}(\omega))\mathbf{V}^x_{\mu\nu}P^q_{\mu\nu}\right] + \sum_{\mu\nu}\left[\mathbf{q}^\dagger(\mathbf{P}^{q})\mathbf{V}^x_{\mu\nu}P^e_{\mu\nu}(\omega)\right] \tag{10}$$

$$\begin{aligned} G'^x_{QM/FQ} = &\sum_{\mu\nu}\left[\mathbf{q}^\dagger(\mathbf{P}^{m})\mathbf{V}^x_{\mu\nu}P^e_{\mu\nu}(\omega)\right] + \sum_{\mu\nu}\left[\mathbf{q}^\dagger(\mathbf{P}^{e}(\omega))\mathbf{V}^x_{\mu\nu}P^m_{\mu\nu}\right] + \\ &+ \sum_{\mu\nu}\left[\mathbf{q}^\dagger(\mathbf{V}^m(\mathbf{P}^e(\omega)))P^x_{\mu\nu}\mathbf{V}_{\mu\nu}\right] + \\ &+ \mathrm{tr}\,\mathbf{P}^e(\omega)G^{mx}(\mathbf{P})_{QM/FQ} = \sum_{\mu\nu}\left[\mathbf{q}^\dagger\mathbf{V}^{m,x}_{\mu\nu}P^e_{\mu\nu}(\omega) + \mathbf{q}^{x\dagger}\mathbf{V}^m_{\mu\nu}P^e_{\mu\nu}(\omega)\right] \end{aligned} \tag{11}$$

2.2 QM/FQ Computational Protocol

Besides the development of the theoretical methodology to actually calculate vibrational spectral signals within the QM/FQ approach, another crucial point of the method is the definition of the QM/FQ model system being investigated. This first implies a sensible choice of the part of the system which is modelled at the QM level. Such a choice can be tricky in case of covalently-bound systems (e.g. in case of a receptor in a protein), however in case of solutions, the most natural choice is to reserve the QM treatment to the solute, and resort to classical physics for the solvent. This basic choice may be possibly refined, so to include a (small) number of solvent molecules in the QM moiety, that based on the analysis of the solute-solvent interaction patterns (e.g. by analyzing the hydrogen-bonding patterns).

The definition of the QM/FQ partition is not the only issue in this kind of modelling. As a matter of fact, the measured spectrum of a given molecular system embedded in a surrounding environment arises from the spectral signals of all the possible configurations spanned by the system. Therefore, in order to get a reliable theoretical description, it is mandatory to reliably take into account both the flexibility of the target QM molecule and the spatial arrangement of the surrounding classical environment, which can evolve in time. The best strategy to do that is to resort to Molecular Dynamics (MD) simulations based on high level force fields (FF), which permit a dynamical description of both the solute flexibility and the solvation phenomenon at the same time.[89,90]

Based on the aforementioned considerations, the QM/FQ computational protocol for the calculation of spectral properties of solvated systems, involves a number of steps:

1. *Definition of the system:* the model systems is composed by the target surrounded by a sufficiently large number of solvent molecules, chosen so that both the dynamics and the subsequent QM/FQ calculations can capture all the relevant solute-solvent interactions.

2. *Classical MD simulations and sampling:* this step is required to sample the phase space of the system. Simulations are run long enough to sample a sufficiently large portion of the phase-space and such that the simulation parameters correctly reproduce all possible system configurations and their relative energy (and thus population). From the MD simulations a number of uncorrelated snapshots are extracted to be used later in the QM/FQ calculations.

3. *Definition of the different regions of the two-layer scheme and their boundaries:* for each snapshot extracted from the dynamics, a sphere centered on the solute is cut, retaining all solvent molecules within the sphere.

4. *Running the QM/FQ calculations on the snapshots:* for each of the spherical snapshots (droplets), IR/Raman/VCD/ROA spectra are calculated, after the geometry of the QM solute is optimized in each snapshot, by keeping fixed the positions/geometries of all the solvent molecules.

5. *Extraction of the average spectra and analysis of the results:* the spectra obtained for each snapshot are extracted and the final IR/Raman/VCD/ROA spectra for the system are obtained as the arithmetic mean of the spectra for all the snapshots.

3 Computational details

Geometry optimization of (L)-Methyl Lactate and (S)-Glycidol was performed at the B3LYP/aug-cc-pVDZ level of theory, by using the conductor-like variant of PCM (C-PCM) to reproduce water bulk solvent effects.[91,92] An analysis of the C-PCM Potential Energy Surfaces(PES) was performed in order to search for the different conformers.

Starting from the most populated C-PCM conformer for both systems, MD simulation was performed to sample the configurational space. Because both molecular systems are flexible, the intramolecular FF was reparametrized. Stiff bonded FF terms (i.e., stretching, bending,

rigid dihedral force constants and equilibrium values) were transferred from the OPLS FF.[93] OPLS Lennard-Jones parameters and CM5 point charges[94] computed on the global minimum were used for the FF nonbonded part. CM5 were chosen because of their tiny dependence on molecular conformations and on the level of theory adopted in the fitting procedure.[94,95] Flexible dihedrals were further re-parametrized by using the Joyce algorithm,[89] by fitting the FF energies of different twisted conformations to their QM counterparts calculated at the B3LYP/aug-cc-pVDZ level. Such conformations were obtained as a results of a relaxed energy scan around the torsion angles of interest, which were varied from 0 to 360 degrees in steps of 30 degrees.

The two molecules, in their lowest C-PCM free energy conformation, were placed in the centre of a cubic box with an edge of 50 Å containing roughly 5000 TIP3P[96] water molecules. Such systems were minimized using the conjugate gradient algorithm until an energy threshold of 0.5 kJ mol^{-1} was reached. Preliminary equilibration steps of 200 ps were performed in the NPT ensemble, using a time step of 0.2 fs. The systems were slowly heated from 150 to 300 K. Berendsen thermostat and barostat were used, with time constants of 0.1 and 1.0 ps, respectively. Periodic boundary conditions were applied in all directions. VdW forces were computed using a cutoff distance of 10 Å. Long-range electrostatic interactions were treated with the particle mesh Ewald (PME) method, using a real-space cutoff radius of 10 Å. Production runs were performed in the NVT ensemble at 300 K. The simulation time was set to 50 ns, and the time step was increased to 2 fs. The LINCS algorithm was used in order to freeze all chemical bonds. Systems coordinates were stored every ps of simulation. All molecular simulations were carried out with the Gromacs 4.6.5 package.[97]

200 uncorrelated snapshots were extracted from the last 40 ns of the MD simulation (one snapshot every 200 ps). For each snapshot a sphere centered at the solute's geometric center was cut, of radius equal to 13 Å. The partial optimization of the QM solute in each snapshot was performed by keeping fixed all water molecules. Finally, IR, VCD, Raman and ROA spectra were calculated with the QM/FQ model, at the B3LYP/aug-cc-pVDZ level

for the solute and the SPC FQ parameters for the FQ portion.[64] All reported spectra were obtained by convoluting peak intensities with a Lorentzian function, with Full Width at Half Maximum (FWHM) of 4 cm^{-1}. Data were finally averaged to obtain the final spectra. All DFT and QM/FQ calculations were performed by using a development version of the Gaussian16 package.[98]

4 Results and Discussion

In this section, the potentialities of the methodology outlined in the previous sections are illustrated by taking as example the calculation of IR, VCD, Raman and ROA spectra of aqueous solutions of (L)-Methyl Lactate (ML) and the (S)-Glycidol (GL). The spectra of the two systems are discussed and compared with experiments, taken from the recent literature.[4,7,74,75,99]

ML and GL are floppy molecules, showing several populated conformers in aqueous solution, possibly separated by low energy barriers.[4,100–105] Therefore, the first step of the simulation protocol is a reliable sampling of such conformations, which will be achieved by resorting to MD runs based on an high level, customized FF.

The subsections reporting on the two systems are structured in the following way: first, conformational analyses and hydration patterns are discussed. Then, vibrational spectra are presented and compared to experiments.

4.1 (L)-Methyl Lactate

4.1.1 Conformational Analysis

Conformers were first located by exploiting the implicit PCM model, at the B3LYP/aug-cc-pVDZ level of theory. Minima geometries were optimized and validated by means of frequency calculations. As expected on the basis of the previous literature,[4,103] three stable conformers were located. Their structures are depicted in Figure 3.

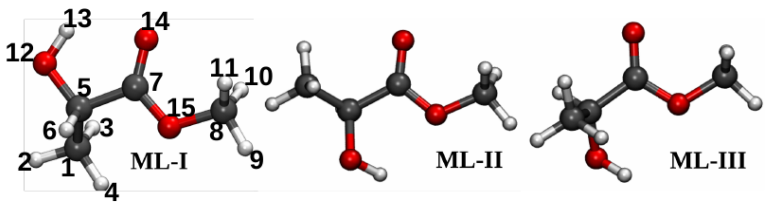

Figure 3: B3LYP/aug-cc-pVDZ/PCM most stable conformers of ML in aqueous solution. ML-I presents also the labeling used in the following.

All PCM minima energy structures are stabilized *via* intramolecular H-bonding interaction between the hydroxyl group and the oxygen of the carbonyl group (ML-I) or of the ester group (ML-II and ML-III). Calculated PCM Boltzmann populations at 298 K are summarized in Table 1, where also the corresponding values obtained in vacuo by Borho et al. at the MP2/aug-cc-pVDZ level of theory are reported.[103]

Table 1: Calculated Boltzmann populations with ZPE corrections included in vacuum (B3LYP/6-311++G(d,p)) and water (B3LYP/aug-cc-pVDZ)

Conformer	Vacuum[103]	Water (PCM)
ML-I	91.8	82.8
ML-II	4.6	9.7
ML-III	3.6	7.5

In order to describe the dynamical fluctuations of the solvent molecules and improve the description of the intermolecular solute-solvent interactions, MD simulations were also performed by starting from the PCM conformers. To properly account for the flexibility of the molecule, a new FF for ML was generated by fitting the potential energy associated to flexible torsion angles with their QM counterpart. In the case of ML, two dihedral angles were considered: i) θ_1, which involves the α hydroxy ester group, and ii) θ_2, which is related to the methyl ester (see Figure 4).

The results of the fitting procedure are reported in Figure 4. The energy profiles associated to θ_1 and θ_2 are very similar and in both cases, the global minimum is located at 0°, while a partial minimum is found at 180°. The minimum found at 0° along θ_1 is not surprising, because the hydroxil group interacts with the carbonyl oxygen *via* intramolecular H-bonding.

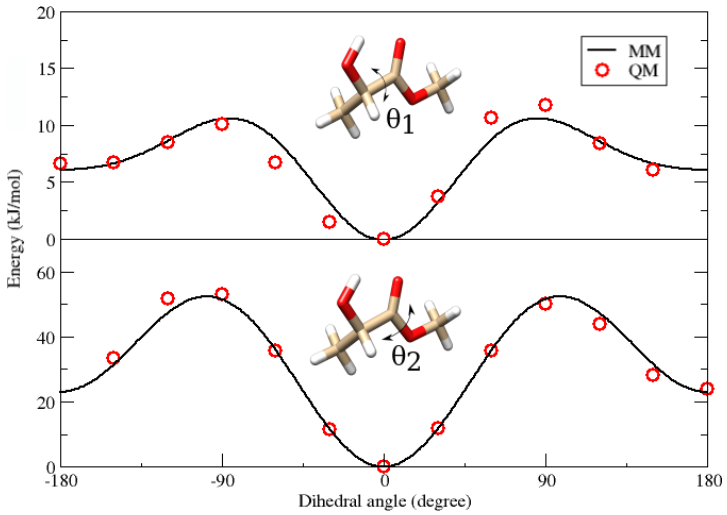

Figure 4: QM (red circles) and MM (black continuous line) potential energy curves along the two dihedral angles θ_1 and θ_2 of ML.

Focusing on the θ_2 angle, the two minima are separated by a high energy barrier of more than 50 kJ·mol^{-1}, whereas the barrier is lower for θ_1 (about 10 kJ·mol^{-1}). Overall, a very good matching between the classical and QM descriptions is noticed, thus supporting the use of the developed FF in the forthcoming MD simulations. The whole FF parameter set is given in Section S1 of the electronic supplementary information (ESI).

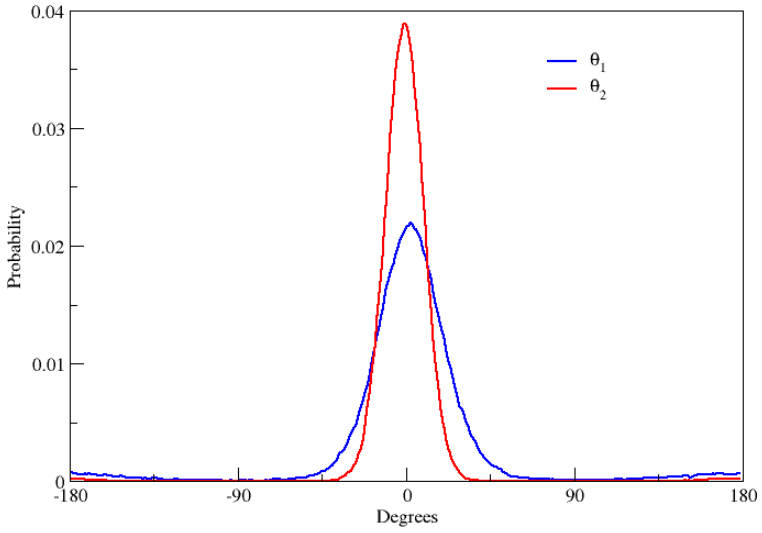

Figure 5: Calculated θ_1 and θ_2 distributions for ML in aqueous solution. The data were extracted from a 50 ns MD simulation exploiting the refined FF (see text).

Figure 5 shows the θ_1 and θ_2 distributions obtained in a 50 ns MD simulation performed

with the refined FF. Clearly, the global minima are well populated with respect to the other possible conformations. Also, a small, but not negligible number of configurations, are generated from the partial minima at 180 degrees.

4.1.2 Hydration Patterns

ML hydration patterns were analyzed by calculating the radial distribution function *g(r)* of water hydrogen and oxygen atoms around the three ML oxygen atoms (O12, O14, O15). The data are reported in Figure 6 (see Figure 3 for the labeling of the atoms).

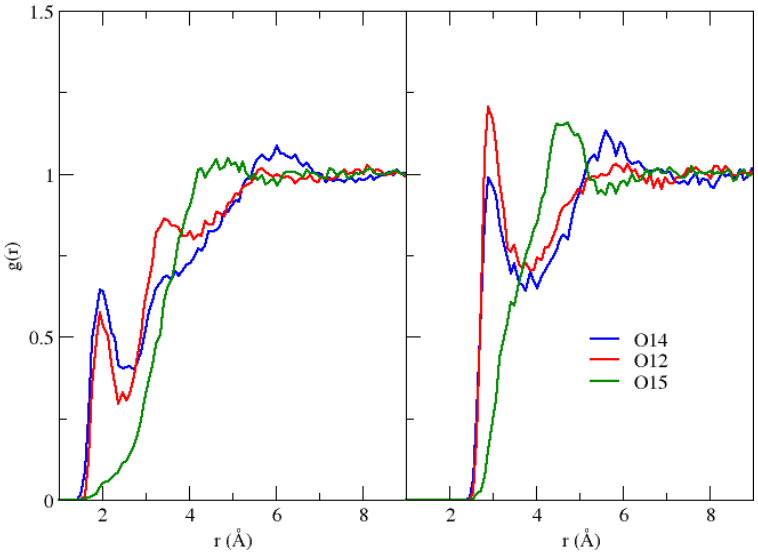

Figure 6: Radial distribution function ($g(r)$) of water hydrogen (left panel) and oxygen (right panel) atoms around the three ML oxygen atoms: O14 (blue line), O12 (red line) and O15 (green line).

In the left panel of Figure 6, the radial distribution functions of water hydrogen atoms around ML oxygen atoms are reported. A well-defined peak at about 2 Å for both carbonyl (O14) and hydroxyl (O12) oxygen atoms is present, thus indicating a strong hydrogen bonding (HB) interaction between ML and the surrounding water molecules. Coordination numbers of approximately 1.30 and 1.04 for O14 and O12 are found, respectively. Thus, a slight preferential HB interaction is reported for the ML carbonyl oxygen atom, if compared to the hydroxyl oxygen. On the contrary, the oxygen atom of the ML alkoxy group (O15, see Figure 6), does not interact with the hydrogen atoms of the surrounding water molecules.

The radial distribution functions related to the interaction of ML with water oxygen atoms are depicted in the right panel of Figure 6; an opposite behaviour with respect to what has been commented above is noticed. In fact, the hydroxyl oxygen atom (O12) can act both as HB donor and HB acceptor: therefore, the water oxygen atoms are placed, on average, preferentially around O12 than around the carbonyl site, O14. We note that our calculated intensities of the $g(r)$) peaks are lower if compared with the data reported in a previous paper,[106] however their relative positions are in good agreement. Such findings show that the here employed electrostatic description of the water solvent (especially the use of the CM5 charges) results in a weaker, albeit well defined, HB interaction of ML with the surrounding solvent.

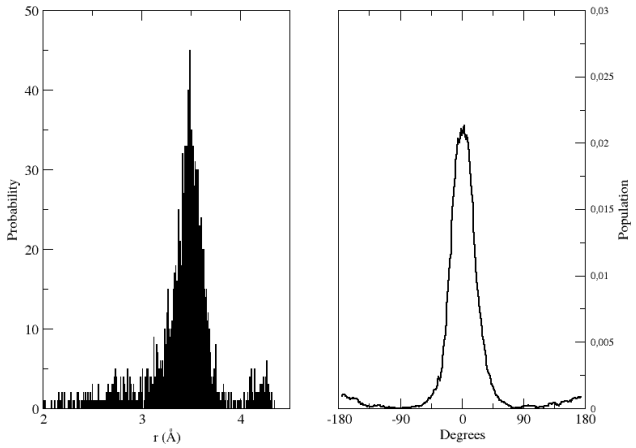

Figure 7: Left panel: H13-O14 distance distribution, sampled in the last 2 ns of simulation time. Right panel: θ_1 distribution, sampled in the last 2 ns of simulation time (right panel).

To end this section, let's focus on the intramolecular HB interaction, which can occur between the ML hydroxyl group and the carbonyl oxygen. Such an interaction is highly favored when the solvent is treated as a continuum dielectric medium (see Table1), in fact the PCM global minimum exhibits an intramolecular *HO-O* distance of 2.052 Å (see Table 1 and Figure 3). In order to check whether this preferential interaction is maintained by the explicit solvent description, the *HO-O* distance during the last 2ns of MD simulation was monitored: the results are plotted in the left panel of Figure 7. Only a small population of conformers exhibit the intramolecular HB interaction. In fact, most conformers show an *HO-O* distance

of about 3.5 Å thus showing that ML-water intermolecular interactions are highly favoured wiht respect to the intramolecular HB by adopting the explicit solvation modeling. As a result, the conformational distribution predicted by exploiting the PCM is expected not to be preserved in the explicit modeling. We also note that our analysis is not biased towards the selection of irrelevant configurations: the θ_1 distribution (see the right panel of Figure 7), which could directly affect the occurrence of intramolecular HB interactions, is in excellent agreement with the corresponding data reported in Figure 5.

4.1.3 IR Spectrum

To calculate the QM/FQ IR spectrum 200 uncorrelated snapshots were extracted from the MD simulation; such a number is enough to yield a converged spectrum, as already pointed out by some of the present authors.[72] The raw data extracted from the single QM/FQ calculations are reported as stick spectrum in Figure S1, given as ESI. Clearly, the overall shape of the final, averaged spectrum is already visible from the data reported in Figure S1 already depicts the shape of the spectrum, also giving insight into the spreading of the vibrational bands, both in wavenumbers and intensities. This is due to the fact that in the different snapshots the spatial distribution of water molecules around ML varies, as well as the conformation of ML.

In order to obtain the final, averaged spectrum, each transition in Figure S1 was convoluted with a Lorentzian function and averaged. The final results are given in (Figure 8), which also shows the experimental spectrum.[4] We first notice that the inhomogeneous band broadening is naturally obtained as a result of the averaging procedure on the stick spectrum. The computed spectrum is characterized by three main bands: 1150 cm^{-1} (bending of the O-CH3 group), 1200-1300 cm^{-1} (composite bending modes, see Figure S2 in the ESI) and 1750 cm^{-1} (CO stretching mode). All the normal modes corresponding to bands in the region 400-1800 cm^{-1} are depicted in Figure S2 in the ESI for a randomly chosen snapshot.

Overall, the calculated spectrum is in very good agreement with the experiment (Figure 8).

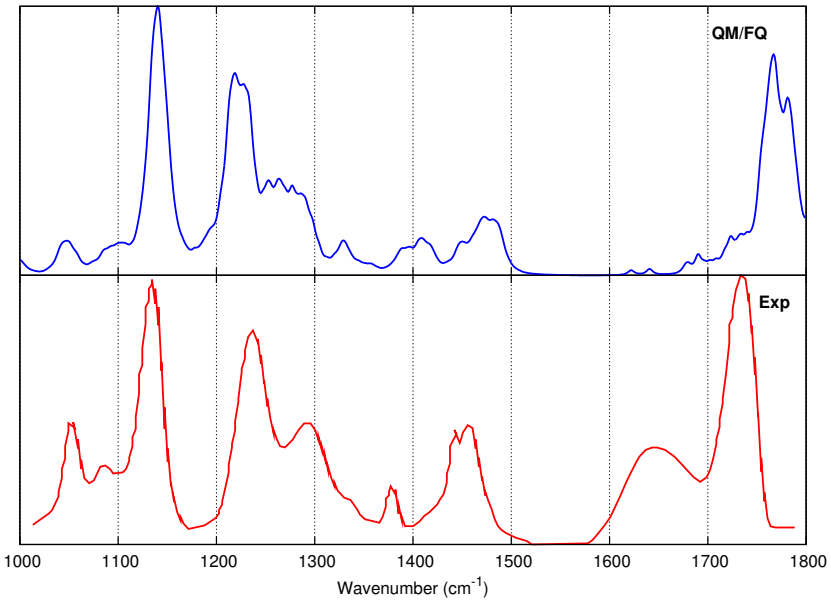

Figure 8: Convoluted QM/FQ IR spectrum of ML in aqueous solution (top). Experimental spectrum taken from Ref.[4] (bottom).

In fact, almost all peaks relative intensities are correctly reproduced, as well as the band broadening. This is particularly evident for the composite band between 1200-1300 cm^{-1}, of which the structure is almost perfectly reproduced. Notice that, as it can be seen from the inspection of the normal models in Figure S2 in the ESI, the vibrational modes causing in this band involve the OH group, which experiences a strong hydrogen bonding interaction with the surrounding water molecules (see the $g(r)$ depicted in Figure 6). The relevance of a correct description of the HB interaction for a correct reproduction of this part of the spectrum is even more emphasized if the results obtained by exploiting a continuum PCM solvent description are considered (See Figure S3 in the ESI). In fact, the PCM completely fails at describing the intensity pattern of this band, due to the lack of the explicit HB interaction in this mean-field approach. Coming back to the the comparison between the QM/FQ and the experimental spectra (see Figure 8), some small discrepancies are indeed present. First, there are small deviations in peak's wavenumbers (especially in the higher energy region), which are due both to the QM level exploited in the calculation, and to the lack of anharmonicity in our calculations. Second, the broad band between 1600-1700 cm^{-1}

is not reproduced by our model. As already reported by some of the present authors[72] and in Refs.,[5–7] this band is attributed to the OH bending mode of water molecules. Our modelling, which focuses on the QM portion of the system only, cannot reproduce such spectral features.

4.1.4 VCD Spectrum

The VCD spectrum of ML was calculated by following the same procedure adopted for the IR spectrum. The computed VCD stick spectrum is plotted in Figure S4, given as ESI. Clearly, the same vibrational normal mode can result in peaks intensities of opposite sign depending on the selected snapshot, i.e. on the particular spatial arrangement of the solvent around the QM molecule and on the specific conformation of the latter. This applies to almost all transitions in the studied region (1000-1800 cm^{-1}). These findings, which have already been pointed out by some of us in previous papers[20,70,72] are particularly remarkable, because in VCD, such as in other chiroptical spectroscopies, it is of crucial importance to correctly reproduce the sign of the single transitions. The data reported in Figure S4 in the ESI confirm the importance of coupling an explicit and dynamic description of the solvation phenomenon (reproduced through MD) with an accurate description of the aqueous solution. The final sign of the bands is obtained as a result of the averaging procedure, of which the results are depicted in Figure 9, where also the experimental spectrum is reported.[4]

The calculated spectrum is characterized by a very intense pattern (+,-,-,-,+) in the region between 1200 and 1500 cm^{-1}. The normal modes involved in these transitions have been discussed before for the IR spectrum. However, it is important to remark that the high negative peak at about 1280 cm^{-1} and the band at 1380 cm^{-1} are due to the bending mode involving the OH group, which, as stated before, interacts with the solvent via hydrogen bonding interactions. Furthermore, the small negative peak between 1700-1800 cm^{-1} is due to the carbonyl stretching.

Figure 9 also reports the experimental spectrum reproduced from Ref.[4] All the signs of the bands and most of the bands relative intensities in the region between 1200-1500 cm^{-1} are

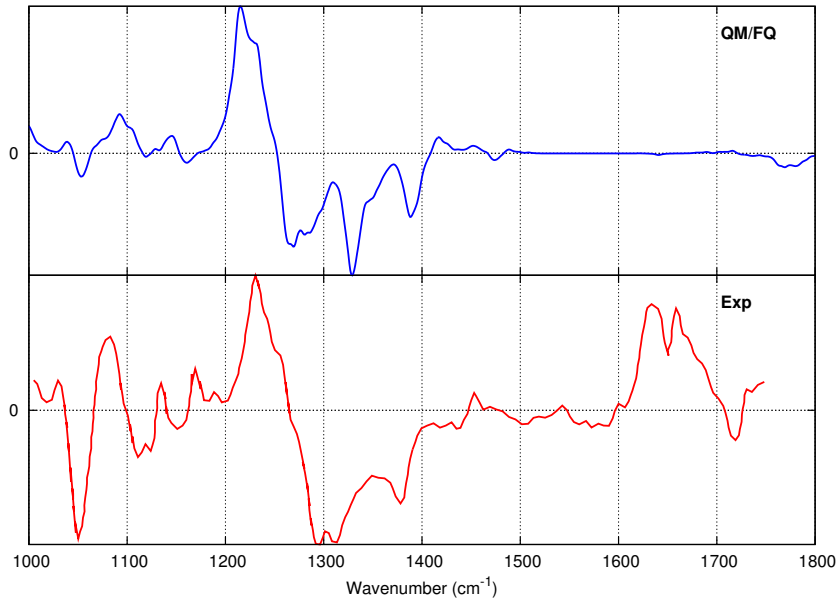

Figure 9: Convoluted QM/FQ VCD spectrum of (L)-Methyl Lactate in aqueous solution (top). Experimental spectrum taken from[4] (bottom).

correctly reproduced in the calculated spectrum. Also, the inhomogeneous band broadening is accurately calculated; this is especially evident for the most intense peak of the spectrum (1220 cm^{-1}), and the negative bands between 1300 and 1400 cm^{-1}. The only region where calculated and experimental data are not in a perfect agreement with the experiment is that below 1200 cm^{-1}; in fact, the computed intensities are too low. The normal modes involved in the regions do not involve any potential site for hydrogen bonding (See Figure S2 in ESI). Therefore, the not perfect reproduction of the experimental spectrum is probably due to the huge alternation of the sign of the bands for the single snapshots in this region, as depicted in Figure S4. Nevertheless, the band sign is correctly reproduced also in this region, as well as the band inhomogeneous broadening. The relevance of exploiting a dynamic explicit solvation modeling for the description of the VCD spectrum of ML is manifest if the results commented above are commented with what can be obtained by resorting to a purely continuum, static QM/PCM approach. In fact, (see Figure S5 given as ESI), the spectral features in the region 1200-1400 cm^{-1} are badly described by the continuum approach: as already discussed, such a range is dominated by vibrational modes directly involving the OH

group, which strongly interacts with the surrounding water molecules as a result of HB (see Figure 6).

To end the discussion on the QM/FQ VCD spectrum of ML, it is worth pointing out that our approach, which focuses on the QM portion only of the multilevel system, cannot reproduce the intense band structure in the 1600-1700 cm^{-1} region; this is not surprising, because such spectral features have been atributed to the so-called "chirality transfer" from water molecules to ML, i.e. they are actually due to water molecules vibrational motions, of which the chiral signal is activated as a result of the interaciton with the chiral ML solute.[5–7]

4.1.5 Raman Scattering Spectrum

The QM/FQ Raman Scattering Spectrum of ML was calculated on the same 200 snapshots extracted from the MD simulation. Figure S6, given as ESI, reports the raw data in the region 400-1800 cm^{-1}. Generally, the same considerations already reported for IR and VCD spectra (Figures S1 and S4) also apply to Raman.

Figure 10 reports the convoluted QM/FQ Raman spectrum and the experimental spectrum.[74] The computed spectrum is characterized by two intense bands at about 830 cm^{-1} and 1500 cm^{-1}, the latter being associated to the bending mode of the O-CH3 moiety. Notice that this normal vibrations has almost zero intensity in the VCD spectrum (see Figure 9), and very low intensity in the IR spectrum (see Figure 8), thus confirming the complementarity of these vibrational spectroscopies in structural studies. The predicted Raman intensities in the region between 1200-1300 cm^{-1}, which correspond to normal modes of groups involved in intermolecular hydrogen bonding interactions, are very low. The same also applies to the most intense peak in the IR spectrum at 1130 cm^{-1}, which exhibits a very low intensity in the Raman spectrum.

Figure 10 also reports the experimental spectrum,[74] for the sake of comparison. Notice that the experimental spectrum of ML in aqueous solution has not been reported in the literature. However, the differences between the neat liquid spectrum (plotted in Figure 10)

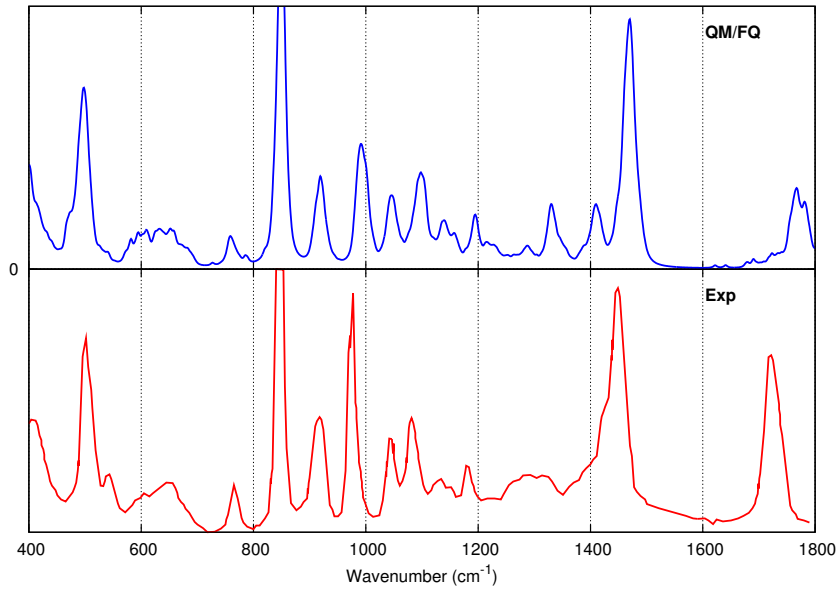

Figure 10: QM/FQ Raman spectrum of ML in aqueous solution (top) and experimental spectrum taken from Ref.[74] (neat liquid, bottom). The external excitation wavelenght is 488 nm.

and the acqueous solution spectra have been discussed,[74] and the major differences have been ascribed to peaks' wavenumbers more than intensities. The comparison of the spectra in Figure 10 shows a very good agreement between calculated and experimental data. In particular, the inhomogeneous band broadening is adequately reproduced for all the bands and relative intensities are also well reproduced, except for the peak at 980 cm^{-1}. This is probably due to the fact that the Raman intensities are not much affected by the presence of the environment, as it is confirmed by the QM/PCM spectrum (see Figure S7 in the ESI), where only small differences between the calculated and the experimental spectra can be appreciated. We finally notice that the reported spectrum is very similar to what was already reported from some of us for the same molecule studied by exploiting a three-layer QM/FQ/PCM approach:[20] clearly, the presence of the third PCM layer is not crucial for the description of the Raman spectral features, and the strong similarity is also a further proof of the little dependence of the calculated spectra on the presence of the external environment.

4.1.6 ROA

Similar to the previous spectra, also the QM/FQ ROA spectrum of ML was calculated on the same 200 snapshots extracted from the MD simulation. Figure S8, given as ESI, reports the raw data in the region 400-1800 cm^{-1}; similar to VCD, the same vibrational normal mode can result in ROA peaks intensities of opposite sign depending on the particular spatial arrangement of the solvent around the QM molecule and on its conformation, as sampled by the MD. This especially applies to the regions below 400 cm^{-1} and between 1100 and 1450 cm^{-1}.

The QM/FQ averaged convoluted spectrum is shown in Figure 11, as well as the experimental spectrum taken from Ref.[107] and measured for the neat liquid. Notice that, as already commented for Raman in the previous section the presence of a third PCM layer[20] is not crucial for the description of the Raman spectral features.

Remarkably, the signs of all peaks are correctly reproduced, as well as their relative intensities and the band broadening, with an accuracy similar to what has already been pointed out for VCD in a previous section. This is not the case of the application of the purely continuum PCM approach (see Figure S9 given in the ESI), which fails at correctly reproducing not ony the band broadening but remarkably the sign of some bands.[20] Therefore, our dynamic computational protocol based on the polarizable QM/FQ approach confirms its remarkable potentialities and reliability for the study of vibrational optical activity spectra.

4.2 (S)-Glycidol

4.2.1 Conformational Analysis

The same protocol as used for ML was exploited to perform (S)-Glycidol (GL) conformational analysis. Thus, it was first performed by describing the aqueous solution by means of the continuum PCM approach, at B3LYP/aug-cc-pVDZ level of theory. GL geometry was optimized, followed by frequency calculations in order to validate the minima struc-

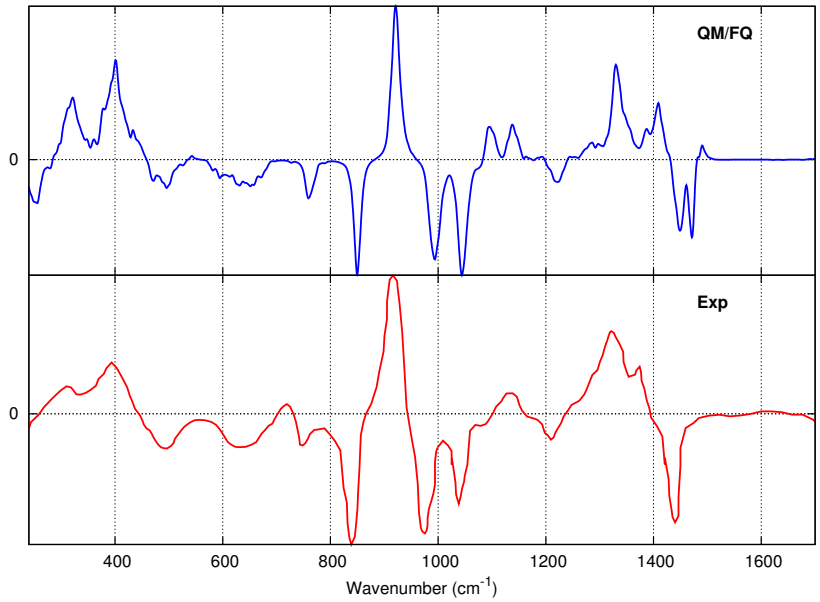

Figure 11: QM/FQ ROA spectrum of ML in aqueous solution (top) and experimental spectrum taken from Ref.[107] (neat liquid, bottom). The external excitation wavelength is 532 nm.

tures. As previously reported in the literature[7,104] eight stable conformers were located; their structures are depicted in Figure 12.

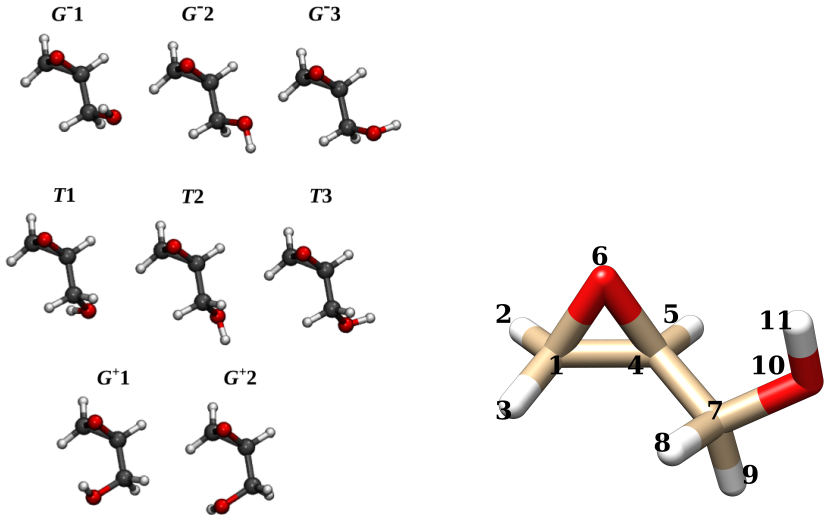

Figure 12: (S)-Glycidol most stable conformers in aqueous solution. In the right panel, the labeling used in the following is reported.

Calculated QM/PCM Boltzmann populations are summarized in Table 2, where also the data calculated in vacuum are reported for the sake of comparison.

We first note that, similarly to ML, the most stable conformers both in vacuo and in solution (G^-1 and G^+1) are stabilized *via* intramolecular H-bonding interaction. Also, solvent effects significantly change the relative populations of the conformers.

Table 2: Calculated B3LYP/aug-cc-pVDZ Boltzmann populations (%) in vacuo and aqueous solution (PCM). ZPE corrections are included.

Conformer	Vacuum	Water (PCM)
G^-1	40.2	31.0
G^-2	3.0	16.0
G^-3	1.8	15.3
$T1$	4.7	7.7
$T2$	3.8	4.2
$T3$	2.8	4.9
G^+1	43.2	17.2
G^+2	0.5	0.7

Remarkably, the population of G^+1 decreases and simultaneously the populations of G^-2 and G^-3 increase. These two conformers are potentially characterized by an intermolecular hydrogen bonding with the solvent molecules (see Figure 3), although this is not explicitly described by the continuum PCM model. In order to improve the conformational analysis by explicitly considering the solvent molecules in their spatial coordinates, MD simulations were performed. To this end, a customized FF for GL was generated by re-parametrizing the flexible torsional coordinate, i.e. the dihedral angle defined by the hydroxyl group and the oxirane moiety. The results of the FF fitting procedure are reported in Figure 13.

Figure 13 clearly shows that the description offered by the refined FF reproduces pretty well the energy profile computed at the B3LYP/aug-cc-pVDZ level. The global minimum is found at approximately -78 degrees, and the other two minima are located at 50 and 150 degrees and separated by an energy barrier of about 10 kJ/mol. The developed FF was further validated by monitoring the dihedral distributions during the 50 ns of MD production run in aqueous solution. As reported in Figure 14, the three different minima along the main dihedral coordinate are selectively populated during the MD simulation. Furthermore, the conformation at -78 degrees is confirmed to be the most populated due to its stability, as

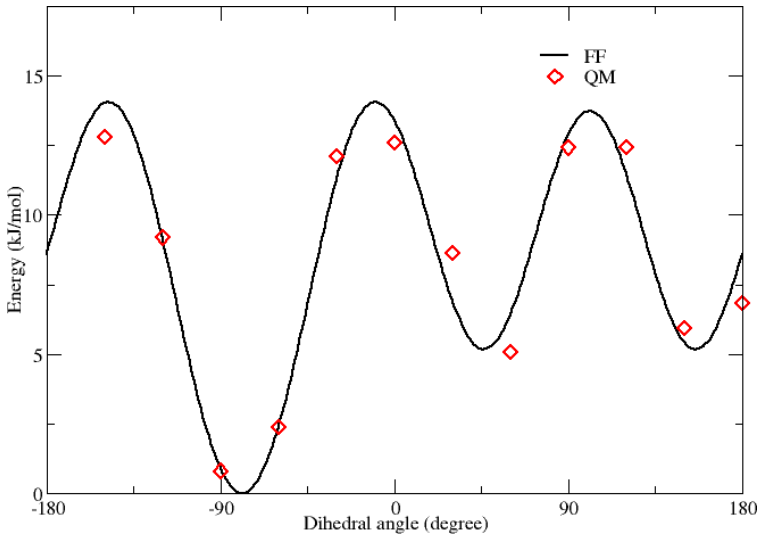

Figure 13: Calculated energy profile along GL flexible dihedral angle. QM (red circles) and fitted FF (black continuous line).

also suggested by the previous QM calculations. The whole GL FF parameter set is given in Section S2.1 of the ESI.

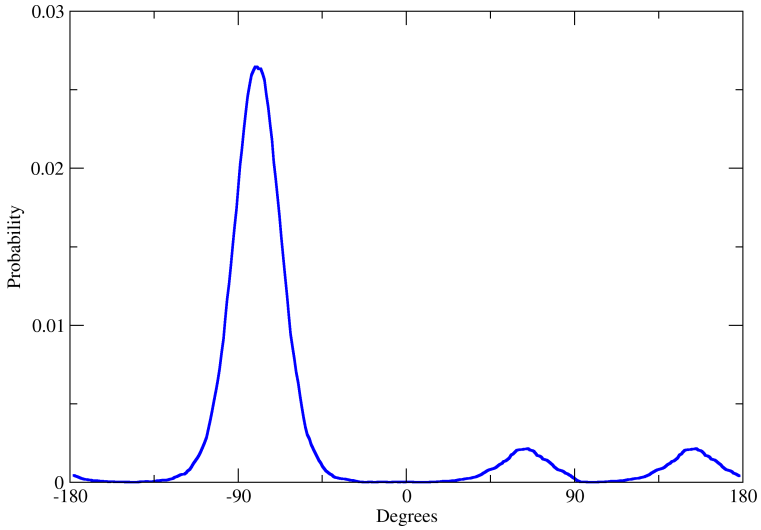

Figure 14: Dihedral distributions of GL in the 50 ns of the MD simulation.

4.2.2 Hydration Patterns

HB patterns were computed for the two GL oxygen atoms O6 and O10 (see Figure 12 for the labeling); their relative $g(r)$ profiles are reported in Figure 15, in which the $g(r)$ distribution

of water hydrogen (left) or oxygen (right) atoms around GL oxygen atoms are reported. Considering the left panel, in the case of O6 the H_w-O_{gly} distribution shows a peak at 1.8 Å, which is more intense then that of the hydroxyl O10, which is located at 1.9 Å. The coordination numbers are 1.3 and 1.08, respectively, thus a clear HB pattern is established between the solute and the solvent molecules. On the contrary, by looking to the right panel of Figure 15, the radial distribution related to of O_w-O_{GL} shows a first peak which is higher in the case of the hydroxyl oxygen O10, that due to this atoms is both HB donor and HB acceptor. The second peak in the O_w-$O6_{GL}$ can be assigned to the water molecules which interact with O10, when O6 and O10 are close to each other. Notice that the results here reported are similar to previuous findings of Xu and coworkers,[7] especially as concerns the position of the peaks. However, the intensity of the O_w-$O10_{GL}$ *g(r)* is remarkably underestimated. This can be once again attributed to the use of CM5 charges, whose absolute values are significantly lower if compared to QM-electrostatic potential derived charges.[108] To confirm such findings, a 50 ns MD with the RESP[109] charge scheme was performed: in this case, the computed $O10_w$-O_{GL} g(r) profile closely reproduces the available literature data (see Figure S10 given as ESI).[7]

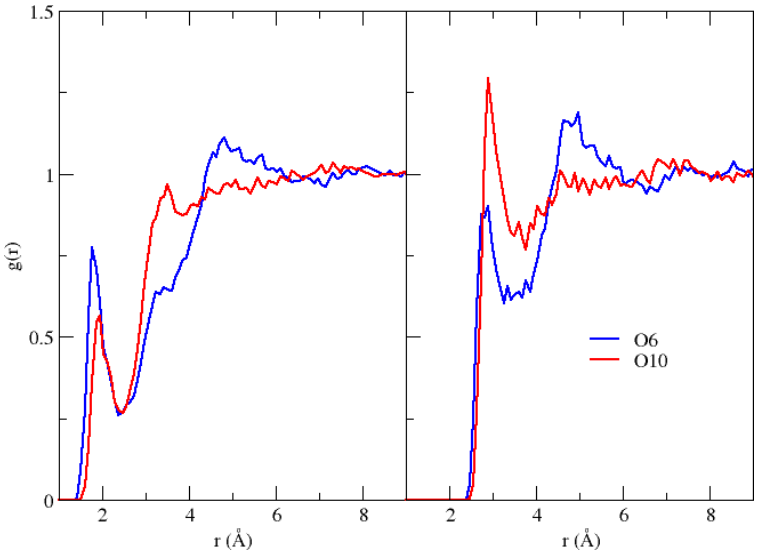

Figure 15: Radial distribution function ($g(r)$) of water hydrogen (left panel) and oxygen (right panel) atoms around the two GL oxygen atoms: O6 (blue line) and O10 (red line).

4.2.3 IR Spectrum

Similar tyo ML, the QM/FQ IR spectrum of GL in aqueous solution was calculated on 200 snapshots extracted from the MD simulation.[72] The raw data extracted form the snapshots are reported in Figure S11 in the ESI. The case of GL is more complicated than ML, because several conformers are present in aqueous solution, as predicted by the MD (see Figure 14). Together with the dynamical description of the solvent molecules and the atomistic description of the QM/FQ model, this conformational flexibility results in a large variability of the peaks of the single snapshots both in intensities and wavenumbers.

Each peak of Figure S11 was convoluted with a Lorentzian function and then averaged in order to obtain the average spectrum in Figure 16, where also the experimental spectrum[7] is reported. The calculated IR spectrum shows an intense peak at about 1050 cm^{-1}, which can be assigned to a diffuse stretching/bending normal mode, involving the hydroxyl group. The composite band between 1200 and 1300 cm^{-1} is mainly constituted by two peaks, the first (1230 cm^{-1}) due to the C-OH bending, the second (1270 cm^{-1}) due to the C-CH bending modes. The computed spectrum also presents a broad band between 1400 and 1500 cm^{-1}, due to C-OH bending (1395 cm^{-1}), a diffuse C-CH bending (1440 cm^{-1}) and a CH_2 bending (1465 cm^{-1}). The normal modes for a randomly chosen snapshot of the MD in the region 700-1800 cm^{-1} are depicted in Figure S12 in the ESI. It is also worth noticing that the variability in the wavenumbers in the stick spectrum (Figure S11) results in the inhomogeneous broadening of the bands in the convoluted spectrum.

The calculated and the experimental spectra are in very good agreement. In fact, most of the relative intensities and the band broadening are correctly reproduced. This is particularly evident for the structured peak between 1200 and 1300 cm^{-1}. Some discrepancies are instead present in the region 1400-1500 cm^{-1} which is characterized in the experimental spectrum by a very broad band. In the QM/FQ spectrum the broadening is not perfectly reproduced due to a not perfect description of the peaks relative intensities, however the three-band structure is correctly described. As for ML, a minor deviation in the vibrational energies due to the

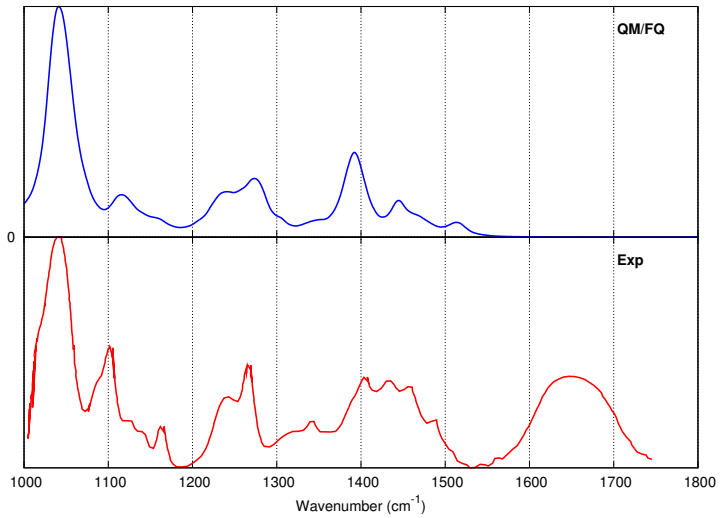

Figure 16: Convoluted QM/FQ IR spectrum of (S)-Glycidol in aqueous solution (top). Experimental spectrum taken from[7] (bottom).

DFT level of theory and to the lack of anharmonicity is reported. Overall, the continuum PCM approach, is inadequate to correctly reproduce the experimental spectrum (see Figure S13 in the ESI), thus remarking once again the huge potentialities of our approach to model vibrational spectra of solutes strongly interacting with the aqueous environment.

To end the discussion on the IR spectrum, we notice that the same broad band between 1600-1700 cm^{-1} already observed for ML is reported also for GL in the experimental spectrum. Obviously, also in this case the focused model cannot reproduce this band.

4.2.4 VCD Spectrum

The QM/FQ VCD spectrum was calculated on the same 200 snapshots extracted from the MD. In Figure S14 the raw VCD data for the different snapshots are depicted. It is worth noticing that almost all spectral regions are characterized by a huge variability in peaks intensities and sign. This behaviour, which has already been discussed for ML, is in this case even more complicated. This is due to the dynamical description of the solvent around GL, but especially to the larger conformational flexibility of GL; the alternation of sign is caused both by the fluctuations of the solvent molecules in time and by the the interconversion

between the several GL conformers.

The convoluted average QM/FQ spectrum is reported together with the experiment[7] in Figure 17. The calculated VCD spectrum is characterized by a (-,+,-,+) sign pattern in the region between 1100 and 1330 cm^{-1}, followed by two negative bands between 1400 and 1550 cm^{-1}. All signs result from the averaging of the sticks in Figure S14 and is it remarkable that such a sing alternation particularly affects the region 1100-1300 cm^{-1}.

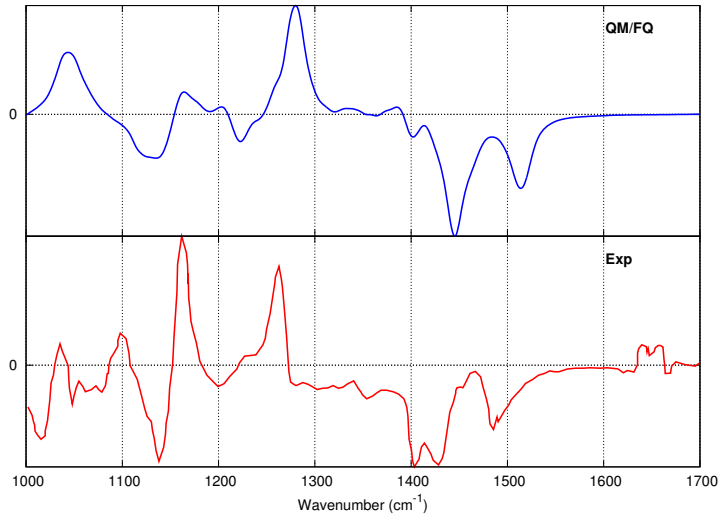

Figure 17: Convoluted QM/FQ (top) and experimental spectrum[7] (bottom) VCD spectrum of GL in aqueous solution.

Moving to the comparison with experimental data (Figure 17) it is worth noticing that most of the experimental signs are correctly reproduced by the QM/FQ model. However, some differences between the computed and the experimental spectra are present and deserve discussion. In fact, the experimentally most intense peak is located at about 1160 cm^{-1}, while the calculated rotational strength in this region is very low. The associated normal mode involves a diffuse mode dominated by the bending of the hydroxyl group, which is hugely affected by the atomistic description of the surrounding water molecules. Moving to the negative peak at about 1220 cm^{-1}, as a matter of fact, the VCD spectrum of GL in CCl_4 solution shows at this frequency a high and positive peak, which becomes negative and with low intensity in aqueous solution.[7] This is the main difference between the spectra

measured in CCl_4 and the H_2O spectrum, thus meaning the this band in the whole VCD spectrum is the most modified by the nature of the surrounding environment. The correct sign reproduction of this peak is one of the most remarkable results achievable by resorting to our discrete model, in which the correct sign results from the averaging of negative and positive sticks in Figure S13. It is also to be noticed that the use of a continuum PCM solvent description (see Figure S15 in the ESI) totally fails to correctly reproduce the sign of this band.

Still on Figure 17, the calculated spectrum in the region between 1400 and 1500 cm^{-1} is in good agreement with the experiment, both sign and intensity. The first intense negative band in this region is experimentally composed by two distinct peaks, while our calculated spectrum reports only a broad band. Probably, the second peak is hidden by the first one (see Figure S14), thus resulting in a broad band instead of two separate peaks.

To end the discussion on the VCD spectrum, we note that the band between 1600-1700 cm^{-1} is again due to chiral imprinting in the solvent molecules, and cannot therefore reproduced with our focused model.

4.2.5 Raman Scattering Spectrum

The Raman spectrum was calculated through analytical evaluation of energy third derivatives.[20] Notice that the same sampling as exploited for the other properties (i.e. 200 snapshots) was exploited, based on previous convergence studies.[20] Raw data calculated at 1064 nm are depicted in Figure S16. Similarly to IR and VCD, also Raman intensities vary as a function of the snapshot. Again, it is worth remarking that this results from the complexity of this molecule, which presents several conformers in aqueous solution and to the atomistic description of the solvent molecules obtained by exploiting the QM/FQ model.

The convoluted calculated spectrum together with experiment[75] is reported in Figure 18. The computed spectrum is characterized by 3 principal bands that can be associated to diffuse normal modes involving O6 and the OH group, and to a diffuse vibration involving

all the atoms in the molecule. Furthermore, two broad bands are predicted in the region 1000-1200 cm^{-1}. Inhomogeneous broadening, particularly evident in the latter bands, occurs from the spreading of the single peaks depicted in Figure S10.

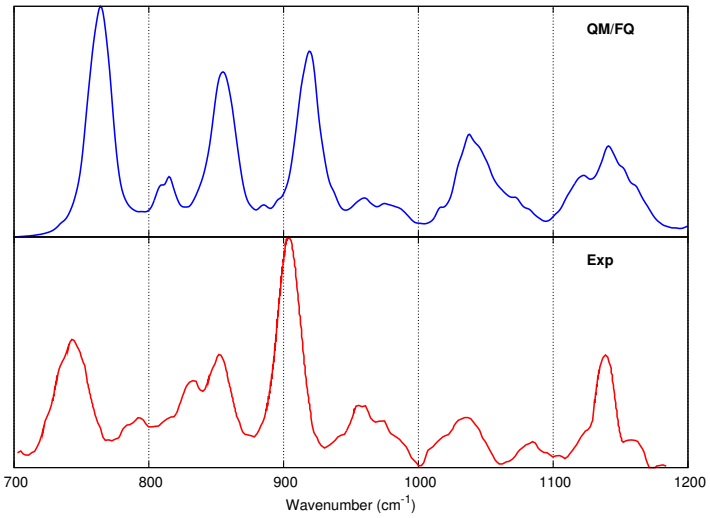

Figure 18: Convoluted QM/FQ (top) and experimental[75] (bottom) Raman spectrum of GL in aqueous solution. Excitation wavelength: 1064 nm

Figure 18 also reports the experimental spectrum, which was measured at 1064 nm.[75] Some differences between the computed and the experimental relative intensities are present. This is particularly evident for the bands at 750, 850 and 900 cm^{-1}, probably due to a not perfect description of the statistical distribution of the several conformations of GL in aqueous solution. However, bands inhomogeneous broadening is almost perfectly reproduced, especially for the small bands at about 800-820 cm^{-1} and above 950 cm^{-1}, which are in almost perfect agreement with the experiment. We note that also for Raman the continuum PCM solvent description (see Figure S17 in the ESI) is not able to correctly reproduce the spectral patterns.

4.2.6 ROA

ROA raw data calculated at 514 nm are depicted in Figure S18 in the ESI. Similarly to VCD, a great variability in peaks intensities and sign is reported.

The convoluted calculated spectrum is reported in Figure 19, together with the experimental spectrum measured for the neat liquid.[99] The computed spectrum is characterized by an intense (-,+,+) pattern that can be associated to diffuse normal modes involving O6 and the OH group.

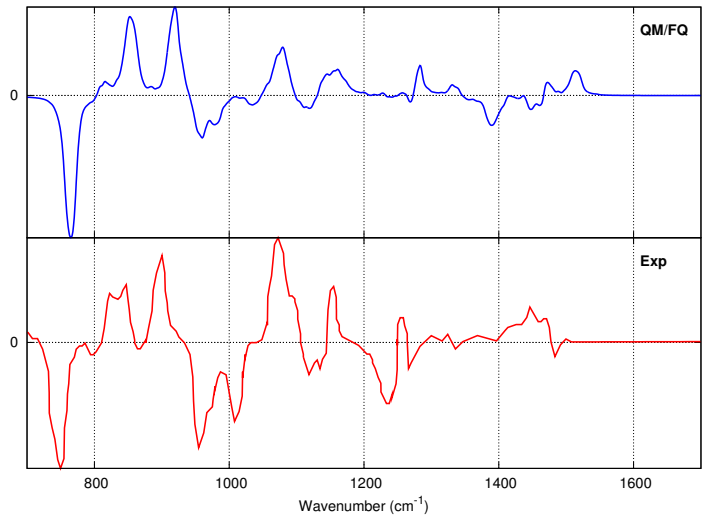

Figure 19: Convoluted QM/FQ (top) and experimental[99] (bottom, neat liquid) ROA spectrum of GL in aqueous solution. Excitation wavelength: 514 nm

Moving to the comparison between calculations and experimental spectra , we note that the relative intensities of the bands between 950 and 1200 cm^{-1} are not perfectly reproduced by our model, however the inhomogeneous band broadening is well described. Such differences are again due to a not perfect description of the statistical distribution of the several conformations of GL in aqueous solution. In addition, the experimental spectrum refers to GL as neat liquid, in which the intermolecular interactions between the GL-GL molecules are largely different from those modelled in our computational sample. Also in this case, the limitations of the continuum PCM approach are evident from the inspection of the spectra reported in Figure S19 in the ESI.

5 Conclusions and Future Perspectives

In this paper, the potentialities of a multi-scale focused approach based on the combination of classical MD simulations and a fully polarizable atomistic QM/FQ Hamiltonian are shown through its application to the calculation of VOA spectra of two chiral systems, able to strongly interact, via hydrogen bonding, with the surrounding aqueous solution. The fully atomistic character of the approach permits a reliable modeling of specific solute-solvent interactions, and the fully account of electrostatic solute-solvent mutual polarization effects yields a reliable description of the solvation phenomenon. Also, the coupling with classical MD simulations permits to account for the solvation dynamics. Remarkably, the application of the method to the calculation of IR, VCD, Raman and ROA spectra of (L)-Methyl Lactate and (S)-Glycidol in aqueous solution shows an excellent agreement between computed and experimental spectra, and of higher quality if compared to standard continuum solvation approaches. Such discrepancies are not only due to the inaccurate description of HB interactions in the continuum approach, but also to a different sampling of the PES resulting from the static PCM or dynamic QM/FQ+MD approaches. Obviously, there is a price to pay for the greatest accuracy. As far as the single QM/FQ calculation on a single snapshot is concerned, the required computational cost is comparable to the corresponding PCM calculation. However, the single calculation needs to be repeated for the number of snapshots required to reach a good modeling of the configurational space, i.e. the final cost of the calculation strongly depends on the number of snapshots which have to be considered to reach the convergence of the desired property. Such a number cannot be defined *a priori*, and especially can wildly vary as a function of the property/spectroscopy to model, from hundreds[20,22,52,71,72] to thousands[70] of representative snapshots.

A limitation of our approach comes from a closer inspection of the IR/VCD spectra of the two systems in the region 1600-1700 cm^{-1}, which was assigned[4,5,5,7] to the bending mode of water molecules bound to the chiral solutes as a result of HB interactions. Interestingly, such bands are also active in the VCD spectra, giving rise to the so-called "chirality transfer"

phenomenon, i.e. the chiral supramolecular arrangement of the achiral solvent molecules around a chiral solute. Such a phenomenon cannot be modelled by our approach, which focuses on the vibrational transitions of the solutes, and their modifications as a result of the interaction with the surroundings. A possible way to extend the model to such phenomena would be to extend the definition of "solute", i.e. including not only the chiral system but a few water molecules in the QM portion, similar to what is done for continuum solvation studies.[110–112] An alternative approach, which appears to be more adequate to our general framework, would be to resort to ab-initio MD[113] techniques coupled to the FQ approach.

As last conclusion, we note that only purely electrostatic solute-solvent interactions have been considered in the current approach. QM/FQ non-electrostatic interactions may play a role and should be included, similar to what has recently been proposed by some of the present authors but to date only limited to the evaluation of energetic properties.[84]

References

(1) Barron, L. D. *Molecular light scattering and optical activity*; Cambridge University Press, 2004.

(2) Nafie, L. A. *Vibrational optical activity: principles and applications*; John Wiley & Sons: Chichester, 2011.

(3) Stephens, P. J.; Devlin, F. J.; Cheeseman, J. R. *VCD spectroscopy for organic chemists*; CRC Press: Boca Raton, 2012.

(4) Losada, M.; Xu, Y. Chirality transfer through hydrogen-bonding: Experimental and ab initio analyses of vibrational circular dichroism spectra of methyl lactate in water. *Phys. Chem. Chem. Phys.* **2007**, *9*, 3127–3135.

(5) Losada, M.; Tran, H.; Xu, Y. Lactic acid in solution: Investigations of lactic acid self-aggregation and hydrogen bonding interactions with water and methanol using vibrational absorption and vibrational circular dichroism spectroscopies. *J. Chem. Phys.* **2008**, *128*, 014508.

(6) Losada, M.; Nguyen, P.; Xu, Y. Solvation of propylene oxide in water: Vibrational circular dichroism, optical rotation, and computer simulation studies. *J. Phys. Chem A* **2008**, *112*, 5621–5627.

(7) Yang, G.; Xu, Y. Probing chiral solute-water hydrogen bonding networks by chirality transfer effects: a vibrational circular dichroism study of glycidol in water. *J. Chem. Phys.* **2009**, *130*, 164506–164506.

(8) Poopari, M. R.; Zhu, P.; Dezhahang, Z.; Xu, Y. Vibrational absorption and vibrational circular dichroism spectra of leucine in water under different pH conditions: Hydrogen-bonding interactions with water. *J. Chem. Phys.* **2012**, *137*, 194308.

(9) Longhi, G.; Castiglioni, E.; Abbate, S.; Lebon, F.; Lightner, D. A. Experimental and calculated CPL spectra and related spectroscopic data of camphor and other simple chiral bicyclic ketones. *Chirality* **2013**, *25*, 589–599.

(10) Berova, N.; Di Bari, L.; Pescitelli, G. Application of electronic circular dichroism in configurational and conformational analysis of organic compounds. *Chem. Soc. Rev.* **2007**, *36*, 914–931.

(11) Polavarapu, P. Ab initio vibrational Raman and Raman optical activity spectra. *J. Phys. Chem.* **1990**, *94*, 8106–8112.

(12) Jose, K. J.; Beckett, D.; Raghavachari, K. Vibrational Circular Dichroism Spectra for Large Molecules through Molecules-in-Molecules Fragment-Based Approach. *J. Chem. Theory Comput.* **2015**, *11*, 4238–4247.

(13) Jose, K. J.; Raghavachari, K. Raman Optical Activity Spectra for Large Molecules through Molecules-in-Molecules Fragment-Based Approach. *J. Chem. Theory Comput.* **2016**, *12*, 585–594.

(14) Barron, L. D. Structure and behaviour of biomolecules from Raman optical activity. *Curr. Opin. Struct. Biol.* **2006**, *16*, 638–643.

(15) Merten, C.; Barron, L. D.; Hecht, L.; Johannessen, C. Determination of the Helical Screw Sense and Side-Group Chirality of a Synthetic Chiral Polymer from Raman Optical Activity. *Angew. Chem. Int. Ed.* **2011**, *50*, 9973–9976.

(16) Kurouski, D.; Lombardi, R. A.; Dukor, R. K.; Lednev, I. K.; Nafie, L. A. Direct observation and pH control of reversed supramolecular chirality in insulin fibrils by vibrational circular dichroism. *Chem. Comm.* **2010**, *46*, 7154–7156.

(17) Oulevey, P.; Luber, S.; Varnholt, B.; Bürgi, T. Symmetry Breaking in Chiral Ionic

Liquids Evidenced by Vibrational Optical Activity. *Angew. Chem. Int. Ed.* **2016**, *55*, 11787–11790.

(18) Ostovar pour, S.; Rocks, L.; Faulds, K.; Graham, D.; Parchaňskỳ, V.; Bouř, P.; Blanch, E. W. Through-space transfer of chiral information mediated by a plasmonic nanomaterial. *Nature Chem.* **2015**, *7*, 591–596.

(19) Stephens, P.; Devlin, F.; Chabalowski, C.; Frisch, M. J. Ab initio calculation of vibrational absorption and circular dichroism spectra using density functional force fields. *J. Phys. Chem.*. **1994**, *98*, 11623–11627.

(20) Giovannini, T.; Olszówka, M.; Egidi, F.; Cheeseman, J. R.; Scalmani, G.; Cappelli, C. Polarizable Embedding Approach for the Analytical Calculation of Raman and Raman Optical Activity Spectra of Solvated Systems. *J. Chem. Theory Comput.* **2017**, *13*, 4421–4435.

(21) Mennucci, B.; Cappelli, C.; Cammi, R.; Tomasi, J. Modeling solvent effects on chiroptical properties. *Chirality* **2011**, *23*, 717–729.

(22) Cappelli, C. Integrated QM/Polarizable MM/Continuum Approaches to Model Chiroptical Properties of Strongly Interacting Solute-Solvent Systems. *Int. J. Quantum Chem.* **2016**, *116*, 1532–1542.

(23) Stephens, P. J. Theory of vibrational circular dichroism. *J. Phys. Chem.* **1985**, *89*, 748–752.

(24) Stephens, P. J. Gauge dependence of vibrational magnetic dipole transition moments and rotational strengths. *J. Phys. Chem.* **1987**, *91*, 1712–1715.

(25) Stephens, P.; Lowe, M. Vibrational circular dichroism. *Ann. Rev. Phys. Chem.* **1985**, *36*, 213–241.

(26) Amos, R.; Handy, N.; Jalkanen, K.; Stephens, P. Efficient calculation of vibrational magnetic dipole transition moments and rotational strengths. *Chem. Phys. Lett.* **1987**, *133*, 21–26.

(27) Stephens, P. J.; Devlin, F. J.; Pan, J.-J. The determination of the absolute configurations of chiral molecules using vibrational circular dichroism (VCD) spectroscopy. *Chirality* **2008**, *20*, 643–663.

(28) Stephens, P.; Devlin, F. Determination of the structure of chiral molecules using ab initio vibrational circular dichroism spectroscopy. *Chirality* **2000**, *12*, 172–179.

(29) Cheeseman, J.; Frisch, M.; Devlin, F.; Stephens, P. Ab initio calculation of atomic axial tensors and vibrational rotational strengths using density functional theory. *Chem. Phys. Lett.* **1996**, *252*, 211–220.

(30) Autschbach, J. Computing chiroptical properties with first-principles theoretical methods: Background and illustrative examples. *Chirality* **2009**, *21*, E116–E152.

(31) Cheeseman, J. R.; Shaik, M. S.; Popelier, P. L.; Blanch, E. W. Calculation of Raman optical activity spectra of methyl-β-d-glucose incorporating a full molecular dynamics simulation of hydration effects. *J. Am. Chem. Soc.* **2011**, *133*, 4991–4997.

(32) Cappelli, C.; Lipparini, F.; Bloino, J.; Barone, V. Towards an accurate description of anharmonic infrared spectra in solution within the polarizable continuum model: Reaction field, cavity field and nonequilibrium effects. *J. Chem. Phys.* **2011**, *135*, 104505.

(33) Cappelli, C.; Corni, S.; Mennucci, B.; Cammi, R.; Tomasi, J. Vibrational Circular Dichroism within the polarizable continuum model: a theoretical evidence of conformation effects and hydrogen bonding for (S)-(-)-3-butyn-2-ol in CCl4 solution. *J. Phys. Chem A* **2002**, *106*, 12331–12339.

(34) Cappelli, C.; Bloino, J.; Lipparini, F.; Barone, V. Toward ab initio anharmonic vibrational circular dichroism spectra in the condensed phase. *J. Phys. Chem.. Lett.* **2012**, *3*, 1766–1773.

(35) Polavarapu, P. L. *Vibrational Spectra: Principles and Applications with Emphasis on Optical Activity: Principles and Applications with Emphasis on Optical Activity*; Elsevier, 1998; Vol. 85.

(36) Corni, S.; Cappelli, C.; Cammi, R.; Tomasi, J. Theoretical approach to the calculation of vibrational Raman spectra in solution within the polarizable continuum model. *J. Phys. Chem. A* **2001**, *105*, 8310–8316.

(37) Cappelli, C.; Corni, S.; Tomasi, J. Electronic and vibrational dynamic solvent effects on Raman spectra. *J. Chem. Phys.* **2001**, *115*, 5531–5535.

(38) Tomasi, J.; Cammi, R.; Mennucci, B.; Cappelli, C.; Corni, S. Molecular properties in solution described with a continuum solvation model. *Phys. Chem. Chem. Phys.* **2002**, *4*, 5697–5712.

(39) Neugebauer, J.; Reiher, M.; Kind, C.; Hess, B. A. Quantum chemical calculation of vibrational spectra of large molecules—Raman and IR spectra for buckminsterfullerene. *J. Comput. Chem.* **2002**, *23*, 895–910.

(40) Reiher, M.; Brehm, G.; Schneider, S. Assignment of vibrational spectra of 1, 10-phenanthroline by comparison with frequencies and Raman intensities from density functional calculations. *J. Phys. Chem. A* **2004**, *108*, 734–742.

(41) Barone, V.; Biczysko, M.; Bloino, J.; Puzzarini, C. Accurate molecular structures and infrared spectra of trans-2, 3-dideuterooxirane, methyloxirane, and trans-2, 3-dimethyloxirane. *J. Chem. Phys.* **2014**, *141*, 034107.

(42) Warshel, A.; Karplus, M. Calculation of ground and excited state potential surfaces of conjugated molecules. I. Formulation and parametrization. *J. Am. Chem. Soc.* **1972**, *94*, 5612–5625.

(43) Warshel, A.; Levitt, M. Theoretical studies of enzymic reactions: dielectric, electrostatic and steric stabilization of the carbonium ion in the reaction of lysozyme. *J. Mol. Biol.* **1976**, *103*, 227–249.

(44) Gao, J. Hybrid quantum and molecular mechanical simulations: an alternative avenue to solvent effects in organic chemistry. *Acc. Chem. Res.* **1996**, *29*, 298–305.

(45) Lin, H.; Truhlar, D. QM/MM: what have we learned, where are we, and where do we go from here? *Theor. Chem. Acc.* **2007**, *117*, 185–199.

(46) Senn, H. M.; Thiel, W. QM/MM methods for biomolecular systems. *Angew. Chem. Int. Ed.* **2009**, *48*, 1198–1229.

(47) Tomasi, J.; Persico, M. Molecular interactions in solution: an overview of methods based on continuous distributions of the solvent. *Chem. Rev.* **1994**, *94*, 2027–2094.

(48) Cramer, C. J.; Truhlar, D. G. Implicit solvation models: equilibria, structure, spectra, and dynamics. *Chem. Rev.* **1999**, *99*, 2161–2200.

(49) Orozco, M.; Luque, F. J. Theoretical methods for the description of the solvent effect in biomolecular systems. *Chem. Rev.* **2000**, *100*, 4187–4226.

(50) Tomasi, J.; Mennucci, B.; Cammi, R. Quantum mechanical continuum solvation models. *Chem. Rev.* **2005**, *105*, 2999–3093.

(51) Pecul, M.; Lamparska, E.; Cappelli, C.; Frediani, L.; Ruud, K. Solvent effects on Raman optical activity spectra calculated using the polarizable continuum model. *J. Phys. Chem. A* **2006**, *110*, 2807–2815.

(52) Egidi, F.; Russo, R.; Carnimeo, I.; D'Urso, A.; Mancini, G.; Cappelli, C. The electronic circular dichroism of nicotine in aqueous solution: a test case for continuum and mixed explicit-continuum solvation approaches. *J. Phys. Chem. A* **2015**, *119*, 5396–5404.

(53) Steindal, A. H.; Ruud, K.; Frediani, L.; Aidas, K.; Kongsted, J. Excitation energies in solution: the fully polarizable QM/MM/PCM method. *J. Phy. Chem. B* **2011**, *115*, 3027–3037.

(54) Day, P. N.; Jensen, J. H.; Gordon, M. S.; Webb, S. P.; Stevens, W. J.; Krauss, M.; Garmer, D.; Basch, H.; Cohen, D. An effective fragment method for modeling solvent effects in quantum mechanical calculations. *J. Chem. Phys.* **1996**, *105*, 1968–1986.

(55) Kairys, V.; Jensen, J. H. QM/MM boundaries across covalent bonds: a frozen localized molecular orbital-based approach for the effective fragment potential method. *J. Phys. Chem. A* **2000**, *104*, 6656–6665.

(56) Halgren, T. A.; Damm, W. Polarizable force fields. *Curr. Opinion Struct. Biol.* **2001**, *11*, 236–242.

(57) Mao, Y.; Demerdash, O.; Head-Gordon, M.; Head-Gordon, T. Assessing Ion–Water Interactions in the AMOEBA Force Field Using Energy Decomposition Analysis of Electronic Structure Calculations. *J. Chem. Theory Comput.* **2016**, *12*, 5422–5437.

(58) Thole, B. T. Molecular polarizabilities calculated with a modified dipole interaction. *Chem. Phys.* **1981**, *59*, 341–350.

(59) Jurinovich, S.; Curutchet, C.; Mennucci, B. The Fenna–Matthews–Olson Protein Revisited: A Fully Polarizable (TD) DFT/MM Description. *ChemPhysChem* **2014**, *15*, 3194–3204.

(60) Boulanger, E.; Thiel, W. Solvent boundary potentials for hybrid QM/MM compu-

tations using classical drude oscillators: a fully polarizable model. *J. Chem. Theory Comput.* **2012**, *8*, 4527–4538.

(61) Loco, D.; Polack, É.; Caprasecca, S.; Lagardere, L.; Lipparini, F.; Piquemal, J.-P.; Mennucci, B. A QM/MM approach using the AMOEBA polarizable embedding: from ground state energies to electronic excitations. *J. Chem. Theory Comput.* **2016**, *12*, 3654–3661.

(62) Curutchet, C.; Muñoz-Losa, A.; Monti, S.; Kongsted, J.; Scholes, G. D.; Mennucci, B. Electronic energy transfer in condensed phase studied by a polarizable QM/MM model. *J. Chem. Theory Comput.* **2009**, *5*, 1838–1848.

(63) Jurinovich, S.; Pescitelli, G.; Di Bari, L.; Mennucci, B. A TDDFT/MMPol/PCM model for the simulation of exciton-coupled circular dichroism spectra. *Phys. Chem. Chem. Phys.* **2014**, *16*, 16407–16418.

(64) Rick, S. W.; Stuart, S. J.; Berne, B. J. Dynamical fluctuating charge force fields: Application to liquid water. *J. Chem. Phys.* **1994**, *101*, 6141–6156.

(65) Rick, S. W.; Stuart, S. J.; Bader, J. S.; Berne, B. Fluctuating charge force fields for aqueous solutions. *J. Mol. Liq.* **1995**, *65*, 31–40.

(66) Stuart, S. J.; Berne, B. Effects of polarizability on the hydration of the chloride ion. *J. Phys. Chem.* **1996**, *100*, 11934–11943.

(67) Lipparini, F.; Cappelli, C.; Barone, V. Linear response theory and electronic transition energies for a fully polarizable QM/classical hamiltonian. *J. Chem. Theory Comput.* **2012**, *8*, 4153–4165.

(68) Lipparini, F.; Cappelli, C.; Scalmani, G.; De Mitri, N.; Barone, V. Analytical first and second derivatives for a fully polarizable QM/classical hamiltonian. *J. Chem. Theory Comput.* **2012**, *8*, 4270–4278.

(69) Lipparini, F.; Cappelli, C.; Barone, V. A gauge invariant multiscale approach to magnetic spectroscopies in condensed phase: General three-layer model, computational implementation and pilot applications. *J. Chem. Phys.* **2013**, *138*, 234108.

(70) Lipparini, F.; Egidi, F.; Cappelli, C.; Barone, V. The optical rotation of methyloxirane in aqueous solution: a never ending story? *J. Chem. Theory Comput.* **2013**, *9*, 1880–1884.

(71) Carnimeo, I.; Cappelli, C.; Barone, V. Analytical gradients for MP2, double hybrid functionals, and TD-DFT with polarizable embedding described by fluctuating charges. *J. Comput. Chem.* **2015**, *36*, 2271–2290.

(72) Giovannini, T.; Olszówka, M.; Cappelli, C. Effective Fully Polarizable QM/MM Approach To Model Vibrational Circular Dichroism Spectra of Systems in Aqueous Solution. *J. Chem. Theory Comput.* **2016**, *12*, 5483–5492.

(73) Gigante, D. M.; Long, F.; Bodack, L. A.; Evans, J. M.; Kallmerten, J.; Nafie, L. A.; Freedman, T. B. Hydrogen stretching vibrational circular dichroism in methyl lactate and related molecules. *J. Phys. Chem. A* **1999**, *103*, 1523–1537.

(74) Cassanas, G.; Morssli, M.; Fabregue, E.; Bardet, L. Vibrational spectra of lactic acid and lactates. *J. Raman Spectrosc.* **1991**, *22*, 409–413.

(75) Badawi, H. M.; Ali, S. A. A study of internal rotations and vibrational spectra of oxiranemethanol (glycidol). *Spectrochim. Acta A* **2009**, *74*, 558–562.

(76) Lipparini, F.; Barone, V. Polarizable force fields and polarizable continuum model: A fluctuating charges/PCM approach. 1. theory and implementation. *J. Chem. Theory Comp.* **2011**, *7*, 3711–3724.

(77) Mortier, W. J.; Van Genechten, K.; Gasteiger, J. Electronegativity equalization: application and parametrization. *J. Am. Chem. Soc.* **1985**, *107*, 829–835.

(78) Rappe, A.; Goddard, W. CHARGE EQUILIBRATION FOR MOLECULAR-DYNAMICS SIMULATIONS. *J. Phys. Chem.* **1991**, *95*, 3358–3363.

(79) Sanderson, R. An interpretation of bond lengths and a classification of bonds. *Science* **1951**, *114*, 670–672.

(80) York, D. M.; Yang, W. A chemical potential equalization method for molecular simulations. *J. Chem. Phys.* **1996**, *104*, 159–172.

(81) Chelli, R.; Procacci, P. A transferable polarizable electrostatic force field for molecular mechanics based on the chemical potential equalization principle. *J. Chem. Phys.* **2002**, *117*, 9175–9189.

(82) Chelli, R.; Schettino, V.; Procacci, P. Comparing polarizable force fields to ab initio calculations reveals nonclassical effects in condensed phases. *J. Chem. Phys.* **2005**, *122*, 234107.

(83) Ohno, K. Some remarks on the Pariser-Parr-Pople method. *Theor. Chim. Acta* **1964**, *2*, 219–227.

(84) Giovannini, T.; Lafiosca, P.; Cappelli, C. A General Route to Include Pauli Repulsion and Quantum Dispersion Effects in QM/MM Approaches. *J. Chem. Theory Comput.* **2017**, *13*, 4854–4870.

(85) McWeeny, R. *Methods of molecular quantum mechanics*; Academic press: London, 1992.

(86) Jin, S.; Head, J. D. Theoretical investigation of molecular water adsorption on the Al (111) surface. *Surf. Science* **1994**, *318*, 204–216.

(87) Calvin, M. D.; Head, J. D.; Jin, S. Theoretically modelling the water bilayer on the Al (111) surface using cluster calculations. *Surf. Science* **1996**, *345*, 161–172.

(88) Biancardi, A.; Cammi, R.; Cappelli, C.; Mennucci, B.; Tomasi, J. Modelling vibrational coupling in DNA oligomers: a computational strategy combining QM and continuum solvation models. *Theor. Chem. Acc.* **2012**, *131*, 1–10.

(89) Cacelli, I.; Prampolini, G. Parametrization and Validation of Intramolecular Force Fields Derived from DFT Calculations. *J. Chem. Theory and Comput.* **2007**, *3*, 1803–1817, PMID: 26627623.

(90) Grimme, S. A General Quantum Mechanically Derived Force Field (QMDFF) for Molecules and Condensed Phase Simulations. *J. Chem. Theory Comput.* **2014**, *10*, 4497–4514, PMID: 26588146.

(91) Cossi, M.; Scalmani, G.; Rega, N.; Barone, V. New developments in the polarizable continuum model for quantum mechanical and classical calculations on molecules in solution. *J. Chem. Phys.* **2002**, *117*, 43–54.

(92) Cossi, M.; Rega, N.; Scalmani, G.; Barone, V. Energies, structures, and electronic properties of molecules in solution with the C-PCM solvation model. *J. Comput. Chem.* **2003**, *24*, 669–681.

(93) Jorgensen, W. L.; Maxwell, D. S.; Tirado-Rives, J. Development and Testing of the OPLS All-Atom Force Field on Conformational Energetics and Properties of Organic Liquids. *J. Am. Chem. Soc.* **1996**, *118*, 11225–11236.

(94) Dodda, L. S.; Vilseck, J. Z.; Cutrona, K. J.; Jorgensen, W. L. Evaluation of CM5 Charges for Nonaqueous Condensed-Phase Modeling. *J. Chem. Theory and Comput.* **2015**, *11*, 4273–4282, PMID: 26575922.

(95) Dodda, L. S.; Vilseck, J. Z.; Cutrona, K. J.; Jorgensen, W. L. Evaluation of cm5 charges for nonaqueous condensed-phase modeling. *J. Chem. Theory Comput.* **2015**, *11*, 4273–4282.

(96) Jorgensen, W. L. Theoretical studies of medium effects on conformational equilibria. *J. Phys. Chem.* **1983**, *87*, 5304–5314.

(97) Pronk, S.; Páll, S.; Schulz, R.; Larsson, P.; Bjelkmar, P.; Apostolov, R.; Shirts, M. R.; Smith, J. C.; Kasson, P. M.; van der Spoel, D.; Hess, B.; Lindahl, E. GROMACS 4.5: a high-throughput and highly parallel open source molecular simulation toolkit. *Bioinformatics* **2013**, *29*, 845–854.

(98) Frisch, M. J.; Trucks, G. W.; Schlegel, H. B.; Scuseria, G. E.; Robb, M. A.; Cheeseman, J. R.; Scalmani, G.; Barone, V.; Petersson, G. A.; Nakatsuji, H.; Li, X.; Caricato, M.; Marenich, A. V.; Bloino, J.; Janesko, B. G.; Gomperts, R.; Mennucci, B.; Hratchian, H. P.; Ortiz, J. V.; Izmaylov, A. F.; Sonnenberg, J. L.; Williams-Young, D.; Ding, F.; Lipparini, F.; Egidi, F.; Goings, J.; Peng, B.; Petrone, A.; Henderson, T.; Ranasinghe, D.; Zakrzewski, V. G.; Gao, J.; Rega, N.; Zheng, G.; Liang, W.; Hada, M.; Ehara, M.; Toyota, K.; Fukuda, R.; Hasegawa, J.; Ishida, M.; Nakajima, T.; Honda, Y.; Kitao, O.; Nakai, H.; Vreven, T.; Throssell, K.; Montgomery, J. A., Jr.; Peralta, J. E.; Ogliaro, F.; Bearpark, M. J.; Heyd, J. J.; Brothers, E. N.; Kudin, K. N.; Staroverov, V. N.; Keith, T. A.; Kobayashi, R.; Normand, J.; Raghavachari, K.; Rendell, A. P.; Burant, J. C.; Iyengar, S. S.; Tomasi, J.; Cossi, M.; Millam, J. M.; Klene, M.; Adamo, C.; Cammi, R.; Ochterski, J. W.; Martin, R. L.; Morokuma, K.; Farkas, O.; Foresman, J. B.; Fox, D. J. Gaussian 16 Revision A.03. 2016; Gaussian Inc. Wallingford CT.

(99) Spencer, K. M.; Edmonds, R. B.; Rauh, R. D. Analytical chiral purity verification using Raman optical activity. *Appl. Spectrosc.* **1996**, *50*, 681–685.

(100) Borba, A.; Gómez-Zavaglia, A.; Lapinski, L.; Fausto, R. Matrix isolation FTIR spectroscopic and theoretical study of methyl lactate. *Vib. Spectrosc.* **2004**, *36*, 79–88.

(101) Freedman, T. B.; Lee, E.; Nafie, L. A. Vibrational transition current density in (S)-

methyl lactate: Visualizing the origin of the methine-stretching vibrational circular dichroism intensity. *J. Phys. Chem. A* **2000**, *104*, 3944–3951.

(102) Aparicio, S. Computational study on the properties and structure of methyl lactate. *J. Phys. Chem. A* **2007**, *111*, 4671–4683.

(103) Borho, N.; Xu, Y. Rotational spectrum of a chiral α-hydroxyester: conformation stability and internal rotation barrier heights of methyl lactate. *Phys. Chem. Chem. Phys.* **2007**, *9*, 1324–1328.

(104) Sun, W.; Wu, J.; Zheng, B.; Zhu, Y.; Liu, C. DFT study of vibrational circular dichroism spectra of (S)-glycidol–water complexes. *J. Mol. Struct.: THEOCHEM* **2007**, *809*, 161–169.

(105) Conrad, A.; Teumelsan, N.; Wang, P.; Tubergen, M. A Spectroscopic and Computational Investigation of the Conformational Structural Changes Induced by Hydrogen Bonding Networks in the Glycidol- Water Complex. *J. Phys. Chem. A* **2009**, *114*, 336–342.

(106) Aparicio, S. Computational Study on the Properties and Structure of Methyl Lactate. *J. Phys. Chem. A* **2007**, *111*, 4671–4683, PMID: 17489567.

(107) Qiu, S.; Li, G.; Wang, P.; Jia, G.; Feng, Z.; Li, C. Hydrogen Bonding in Homochiral Dimers of Hydroxyesters Studied by Raman Optical Activity Spectroscopy. *J. Raman Spectrosc.* **2012**, *43*, 503–513.

(108) Dupradeau, F.-Y.; Pigache, A.; Zaffran, T.; Savineau, C.; Lelong, R.; Grivel, N.; Lelong, D.; Rosanski, W.; Cieplak, P. The REd. Tools: Advances in RESP and ESP charge derivation and force field library building. *Phys. Chem. Chem. Phys.* **2010**, *12*, 7821–7839.

(109) Bayly, C. I.; Cieplak, P.; Cornell, W.; Kollman, P. A. A well-behaved electrostatic potential based method using charge restraints for deriving atomic charges: the RESP model. *J. Phys. Chem.* **1993**, *97*, 10269–10280.

(110) Barone, V.; Cimino, P.; Pedone, A. An integrated computational protocol for the accurate prediction of EPR and PNMR parameters of aminoxyl radicals in solution. *Magn. Reson. Chem.* **2010**, *48*, S11–S22.

(111) Stendardo, E.; Pedone, A.; Cimino, P.; Menziani, M. C.; Crescenzi, O.; Barone, V. Extension of the AMBER force-field for the study of large nitroxides in condensed phases: an ab initio parameterization. *Phys. Chem. Chem. Phys.* **2010**, *12*, 11697–11709.

(112) Cappelli, C.; Mennucci, B.; Monti, S. Environmental effects on the spectroscopic properties of gallic acid: a combined classical and quantum mechanical study. *J. Phys. Chem. A* **2005**, *109*, 1933–1943.

(113) Scherrer, A.; Vuilleumier, R.; Sebastiani, D. Nuclear velocity perturbation theory of vibrational circular dichroism. *J. Chem. Theory Comput.* **2013**, *9*, 5305–5312.